



PONTIFICIA UNIVERSIDAD CATÓLICA DE CHILE
ESCUELA DE INGENIERÍA

INVESTIGATION ON TIDAL TURBINE ARRAYS WITH A COUPLED DES-BEM MODEL

DANIEL IGNACIO GAJARDO ORELLANA

Thesis submitted to the Office of Research and Graduate Studies
in partial fulfillment of the requirements for the degree of
Master of Science in Engineering

Advisor:

CRISTIÁN ESCAURIAZA MESA

Santiago de Chile, August 2017

© MMXVII, DANIEL IGNACIO GAJARDO ORELLANA



PONTIFICIA UNIVERSIDAD CATÓLICA DE CHILE
ESCUELA DE INGENIERÍA

INVESTIGATION ON TIDAL TURBINE ARRAYS WITH A COUPLED DES-BEM MODEL

DANIEL IGNACIO GAJARDO ORELLANA

Members of the Committee:

CRISTIÁN ESCAURIAZA MESA

RODRIGO CIENFUEGOS CARRASCO

DAVID M. INGRAM

ÁNGEL ABUSLEME HOFFMAN

Thesis submitted to the Office of Research and Graduate Studies
in partial fulfillment of the requirements for the degree of
Master of Science in Engineering

Santiago de Chile, August 2017

© MMXVII, DANIEL IGNACIO GAJARDO ORELLANA

To my parents and sisters

ACKNOWLEDGEMENTS

I would like to thank my family for the unconditional support they have given me in every single project I have embarked on. This thesis is dedicated to my parents, Pilar and Héctor, and my sisters, Pili and Coti, who have taught me to try my best in everything I do, to look at challenges with optimism, and to cherish happiness throughout my life. Without their energy and love I would not be the person who I am now.

I am deeply grateful to my advisor, Cristián Escauriaza, whose views on life have made this research experience not only one of professional development, but also one of personal knowledge and growth. I thank him for his trust in me and my work, giving me continuous chances to prove my abilities and enhance my skills. His profound and challenging questions pass on a passion for caring about the meaning and impact of our work.

Special gratitude to Professor David Ingram, for receiving me in the University of Edinburgh and agreeing to guide my work. He motivated me with my research, making me understand the implications and potential of my project. He helped me articulate my research from a global perspective, making it fit in a complex environment where academy, governments and developers are pushing tidal energy forward.

On a personal level, I kindly thank all my friends that have accompanied me during my university process. Unfortunately I cannot name them all, but it has been a privilege to share so many moments with you. Thanks for being there in both happy and sad times, for all the advice you have given me, and for your constant disposition to share and build memories. I would like to specially mention my friends in the Hydraulics and Environmental Engineering Department, for joining me in all the ups and downs of graduate student life.

My life as a student was changed by two projects I would like to thank. Both of them involve sharing expectations, dreams and passions, and working in order to make the places where we live a better place. First, I would like to thank everyone involved in the *Centro de Alumnos de Ingeniería 2014*, for that year where we freely put our time and dedication to make our School an active and inclusive community. Second, I express my gratitude to all the co-founding team of Engineers Without Borders Chile, hopefully when years go by we will have contributed to making engineering in Chile stand out for its social role.

I thank the comments provided by Dr. Angus Creech to this study, essential for the turbine representation model. This work has been supported by Fondecyt project 1130940, by CONICYT grants 80160084 and 22160577, and by Chile's Marine Energy Research & Innovation Center (MERIC) CORFO project 14CEI2-28228. The study was partially supported by the RC UK Energy Programmes UK Centre for Marine Energy Research (EP/I027912/1). Powered@NLHPC: This research was partially supported by the super-computing infrastructure of the NLHPC (ECM-02).

TABLE OF CONTENTS

ACKNOWLEDGEMENTS	iv
LIST OF FIGURES	viii
LIST OF TABLES	xi
ABSTRACT	xii
RESUMEN	xiv
1. INTRODUCTION	1
2. METHODOLOGY	6
2.1. Detached-Eddy Simulation	7
2.2. Blade Element Momentum	8
2.3. Unsteady inlet	13
2.4. Analysis variables	14
2.4.1. Velocity field	14
2.4.2. Turbulence statistics	14
2.4.3. Vortex visualization	15
2.4.4. Bed shear stress	15
2.4.5. Power and thrust coefficients	15
3. PERAWAT CASE STUDY	17
3.1. Flume and turbine geometry	17
3.2. Arrays studied	18
3.3. Grids	18
3.4. Boundary conditions	21
4. RESULTS	22
4.1. Single turbine	22

4.1.1.	Mean flow field	22
4.1.2.	Instantaneous flow field	26
4.2.	Arrays	27
4.2.1.	Mean flow field	27
4.2.2.	Instantaneous flow field	30
4.2.3.	Effects on the bed	32
4.2.4.	Performance measurements	35
5.	CONCLUSIONS AND FUTURE RESEARCH	38
	REFERENCES	41
	APPENDIX	48
A.	Random Flow Generation Technique	49
B.	Flow statistics for the aligned rows case	52
C.	Turbulence statistics for the staggered rows case	53
D.	Effects on the bed for the staggered rows array	54
E.	Turbine performance for doubled row arrays	55

LIST OF FIGURES

2.1	Schematic view of the cylindrical turbine volume V , with radius R and length L . Mesh nodes inside it are used for calculating the body forces that are passed to the Navier-Stokes equations in the DES model.	6
2.2	Overview of every time-step calculation procedure.	7
2.3	Frontal view of the variables used in Blade Element Momentum.	9
2.4	Blade section view of the variables involved in the lift and drag decomposition of Blade Element Momentum.	9
3.1	Schematic representation of (a) single turbine case; (b) two staggered rows array and (c) two aligned rows array. Like in the single turbine case, the central turbine of the first row in (b) and (c) is located at the vertical and lateral center of the flume, and at a distance of $5D$ downstream from the inlet. Lateral spacing between devices is the same in every array. The figures are not to scale, so devices seem much closer to flume walls than in the actual experiments, where turbines are far from them and can be considered to be operating without the influence of the flume's lateral boundaries.	19
3.2	Grid used for the two staggered row case.	20
4.1	Lateral and longitudinal plots of axial velocity. (a) Lateral profiles of velocity deficit for the single turbine case. The difference between the curves is explained because of the limitations of BEM applications and our simplification of not simulating the complete hub, nacelle and support structure geometry; (b) Axial velocity profile along the hub axis for a single turbine. Velocity tends to be underestimated in approximately 10% by the DES-BEM model, but both curves show the same rate of recovery.	23

4.2	Contour plots of mean flow statistics at a vertical plane at $y/D=0$ for the single turbine case: (a) non-dimensional mean longitudinal velocity; (b) non-dimensional mean transverse velocity; (c) non-dimensional mean axial vorticity.	25
4.3	Contour plots of turbulence statistics at a vertical plane at $y/D=0$ for the single turbine case: (a) non-dimensional TKE; (b) non-dimensional principal Reynolds shear stress.	26
4.4	Plots of q iso-surfaces for the single turbine case. (a) three dimensional view; (b) superior view.	27
4.5	Lateral profiles of mean velocity deficit, with distance measured from the second row of turbines. (a) two staggered rows; (b) two aligned rows. The BEM-DES simulations show good agreement with the experimental data even in the near wake region, with predictions being better than the BEM-URANS application.	28
4.6	Axial profiles of mean longitudinal velocity downstream of the second row of the two aligned rows array, with velocity taken at hub height. Continuous lines represent BEM-URANS results, dashed lines are our DES-BEM results and isolated icons represent experimental results. After $2D$ downstream the DES-BEM improves the representation on profile evolution, matching the experimental data.	29
4.7	Contour plots of mean flow statistics at a horizontal plane at $z/D = 0$ for the two staggered rows case: (a) non-dimensional mean longitudinal velocity; (b) non-dimensional mean vertical velocity; (c) non-dimensional mean axial vorticity.	31
4.8	Contour plots of turbulence statistics at a vertical plane at $y/D=0$ for the single turbine case: (a) non-dimensional TKE; (b) non-dimensional principal Reynolds shear stress.	32

4.9	Plots of q -isosurfaces for the studied arrays. (a),(c): two staggered rows; (b),(d): two aligned rows.	33
4.10	Contour plots of u_* and $u_{*,rms}$ for the ten turbine array: (a) time-averaged shear velocity, (b) shear velocity RMS.	34
4.11	Box plots for C_P . Each box plot is obtained with the timeseries of the respective turbine in the array. Superior plots are for frontal rows, and inferior for posterior ones. (a) two staggered rows; (b) two aligned rows.	36
4.12	Box plots for C_T . Each box plot is obtained with the timeseries of the respective turbine in the array. Superior plots are for frontal rows, and inferior for posterior ones. (a) two staggered rows; (b) two aligned rows.	36
B.1	Contour plots of mean flow statistics at a horizontal plane at $z/D = 0$ for the aligned rows case: (a) non-dimensional mean longitudinal velocity; (b) non-dimensional mean vertical velocity; (c) non-dimensional mean axial vorticity.	52
C.1	Contour plots of turbulence statistics at a horizontal plane at $z/D = 0$ for the staggered rows case: (a) non-dimensional TKE; (b) non-dimensional principal Reynolds shear stress.	53
D.1	Contour plots of u_* and $u_{*,rms}$ for the staggered rows array: (a) time-averaged shear velocity, (b) shear velocity RMS.	54

LIST OF TABLES

3.1	Principal turbine parameters for the studied test case.	18
3.2	Details of the parameters used for the computational meshes. N_i and Δi indicate the number of nodes and spacing in the i direction, respectively. (L/D) represents the cylindrical length of the turbine volumes with respect to turbine diameter.	20
3.3	Minimum and maximum number of nodes inside the turbine volumes for every studied array.	20
E.1	Turbine performance results for the two double row arrays. Statistics are obtained averaging the desired variable for every device on the same row. The comparison between arrays is performed by calculating the ratio between the variability of both arrays.	55

ABSTRACT

In order to develop tidal current energy, the effect turbines have on their surrounding flow and how these devices perform when installed in an array need to be better understood. This requires studying the hydrodynamics related to tidal turbines and their wakes. Detailed information on flow characteristics is needed to comprehend wake interaction and changes on the ambient flow due to tidal turbines. However, there have been limited approaches that are able to analyze multiple tidal turbines simultaneously. Here we propose a numerical methodology that couples Blade Element Momentum (BEM) with Detached-Eddy Simulation (DES) to simulate tidal turbine arrays and obtain detailed information on the mean and instantaneous flow. Simulations are carried out using real rotor data and validated with existing experimental and modeled results on three different array configurations. The model shows good correlation with experimental mean flow profiles and turbine performance measurements. We show that wakes of downstream turbines are characterized by higher levels of turbulence and temporal fluctuations than upstream turbine ones. Downstream regions show higher levels of turbulent kinetic energy and Reynolds stresses, along with stronger presence of vortical structures. The more complex flow faced by downstream turbines produced lower power and thrust coefficients on them. Moreover, performance measurements and induced bed shear stress showed considerably higher temporal fluctuations for posterior rows in the studied arrays. These results help understand the behavior of turbines in an array and how their performance and impacts change when devices function together. Furthermore, the proposed methodology is validated for its use on different array configuration and turbine designs.

Keywords: DES, BEM, tidal turbines, turbulence, tidal energy.

RESUMEN

Para desarrollar la energía de corrientes de marea es necesario comprender el efecto que las turbinas marinas tiene sobre su entorno y cómo estos dispositivos se desempeñan cuando son instalados en un arreglo. Esto requiere estudiar la hidrodinámica asociada a las turbinas marinas y sus estelas, con información detallada de las características del flujo. Sin embargo, han habido limitados estudios capaces de analizar múltiples dispositivos simultáneamente. En este estudio proponemos una metodología numérica que acopla *Blade Element Momentum* (BEM) con *Detached-Eddy Simulation* (DES) para simular arreglos de turbinas marinas y obtener información detallada del flujo promedio e instantáneo. Se simularon tres configuraciones de arreglos distintas utilizando datos de turbinas reales, utilizando resultados experimentales y numéricos para validar el modelo propuesto. Los resultados muestran buena correlación con perfiles de velocidad promedio y mediciones del desempeño de las turbinas. Se muestra que las estelas de turbinas ubicadas aguas abajo en el arreglo están caracterizadas por mayores niveles de turbulencia, enfrentando flujos dominados por estructuras coherentes de gran escala. Este flujo más complejo produce que turbinas aguas abajo tengan menores coeficientes de potencia y de empuje. Además, las medidas de desempeño y el efecto de corte sobre el fondo mostraron una fluctuación temporal considerablemente más importante en las filas posteriores de los arreglos estudiados. Estos resultados permiten comprender el comportamiento de turbinas en arreglos, y cómo su desempeño e impactos cambian cuando varios dispositivos operan simultáneamente. Se espera que la metodología validada sea utilizada para estudiar nuevos arreglos de turbinas y nuevos diseños de dispositivos, permitiendo avanzar en el desarrollo de la energía de corrientes de marea.

Palabras Claves: DES, BEM, turbinas marinas, turbulencia, energía marina.

1. INTRODUCTION

Increasing energy demand and the growing concern about climate change have been major drivers for the development of renewable energies during the last decade (Edenhofer et al., 2012). Among them, using tidal streams constitutes one of the most promising alternatives for generating clean and reliable energy in the years to come. The high predictability of tidal periods and amplitudes make this technology trustworthy and attractive for electricity generation (Lynn, 2014; Magagna & Uihlein, 2015). Between the various design approaches for extracting the tidal energy resource, Horizontal Axis Tidal Turbines (HATTs) are the frontrunners, concentrating most of the research and investments being made in the sector (Magagna & Uihlein, 2015; Yuce & Muratoglu, 2010; Khan et al., 2009). Nevertheless, there are still myriad challenges that policy-makers, researchers and developers must solve before deploying this type of marine hydrokinetic (MHK) devices in large numbers, with complete understanding of the implications of such installation (Magagna & Uihlein, 2015; Yuce & Muratoglu, 2010; Uihlein & Magagna, 2016).

Polagye et al. (2010) states that HATTs will affect flows in tidal channels, because they will extract energy and generate regions of higher turbulence and velocity deficits downstream from them, known as turbine wakes. Therefore, the new flow regime after the extraction of energy will have changed both its hydrodynamic conditions and the nature of its tidal resource (Bryden & Couch, 2006). This can have environmental consequences like changes in the tidal range and sediment transport, and also affect the energy production of devices installed in this new flow regime. Thus, it is crucial to fully understand how HATTs interact with the flow in which they are placed and also how they interact between them. The latter point is specially relevant because, most likely, tidal generation will involve multiple devices installed in an array form.

To study these interactions it is necessary to assess the hydrodynamics that underlie the operation of HATTs over the wide range of length and time scales involved. For example, tidal turbines interact with turbulent structures in the scale of basins and ocean tides, but

are also affected by small scale phenomena associated with turbulent effects in the scale of turbine blades. Experimental approaches have been put forward to do this, but most of the research is limited to analyzing only one device. For example, Chamorro et al. (2013) carried out an experimental analysis of a single scaled turbine. They concluded that power production is highly linked to the turbulent features on the incoming flow and described a meandering motion in the turbine wake that had only been previously reported on wind turbines. Gaurier et al. (2013) performed flume tests on a three bladed HATT, showing that waves can amplify the loadings devices have to cope with, and emphasized the need to better understand wave-current interaction with tidal devices. Mycek et al. (2014b) performed experimental tests to study how different ambient turbulence levels change turbine operation and wake development, showing how turbulence modifies wake shape, length and strength, while also changing performance.

There have been fewer efforts to study turbine arrays on an experimental level. Stalard et al. (2013) conducted experiments with up to ten scaled turbines on several array configurations, discussing the effects on the wake of lateral and longitudinal spacing between devices. They underscore the importance of array configuration on wake recovery. Myers & Bahaj (2012) used porous discs to experimentally represent tidal turbines in arrays, showing that wake interaction can cause an increase in turbine loading and decrease power production on downstream devices. Mycek et al. (2014a) studied two interacting turbines aligned with the flow, and concluded that higher turbulence intensity levels can improve the operation of the downstream turbine by accelerating the rate of recovery for the upstream turbine wake. These studies underscore that turbines alter their performance and hydrodynamics when interacting with other wakes. Even though these experimental studies provide essential insights, they are limited to physical constraints of laboratory conditions, can be expensive to perform and are not able to measure data in the entirety of the spatial and temporal domain.

Since HATTs in an array do not perform as if they were isolated, arrays must be analyzed as a whole. Therefore, there is a need for methodologies that can provide both

the ability to study multiple devices at the same time while also reporting information on unsteady and turbulent flows. Numerical simulations emerge as an attractive alternative to do this, because test conditions can be easily modified and they can improve the detail in which information is gathered. Considering this, the objective of our work is to validate a numerical methodology for analyzing large turbine arrays, and give insight into turbine-turbine and turbine-flow interaction.

In order to numerically represent tidal turbines, models range from simpler actuator disk models (ADMs), to higher complexity approaches like actuator line models (ALMs) or solving the full turbine geometry. The first ones apply a uniform force to the flow and are computationally cheap allowing them to consider multiple devices simultaneously, but lose the representation of important elements like rotor swirl (Nguyen et al., 2016; Batten et al., 2013; Blackmore et al., 2014). The latter ALMs and solved geometry models improve turbine representation, but require considerably more computational resources, and therefore have not been used for large turbine arrays (Creech et al., 2017; Afgan et al., 2013; Lloyd et al., 2014; Churchfield et al., 2013; Pinon et al., 2012; Kang et al., 2014; Chawdhary et al., 2017).

Blade Element Momentum (BEM) models are a middle ground between the approaches mentioned before. They incorporate rotational components into the flow, smearing the effect of turbine blades onto an actuator volume, but are not able to represent discrete blade effects like tip vortices. They have been widely used to represent tidal and wind turbines, showing overall good representation of wake hydrodynamics (Masters et al., 2011; Edmunds et al., 2017; Masters et al., 2013). It is important to note that, as demonstrated by Kang et al. (2014), not considering the full turbine geometry does not produce essential vortical structures that dominate the evolution of turbine wakes. We acknowledge and consider these limitations of a lower-order model like BEM, but still argue that their application remains useful and needed for studying turbine arrays, and can provide information for understanding turbine hydrodynamics.

To solve the flow field associated with tidal turbines, models like BEM must be coupled with Computational Fluid Dynamics (CFD) solvers. Simple approaches use Reynolds-Averaged Navier-Stokes (RANS) equations (Nguyen et al., 2016; Batten et al., 2013; Afgan et al., 2013; Edmunds et al., 2017), but since RANS simulates turbulence by dissipating velocity fluctuations, it cannot predict unsteady features such as large scale vortices that have been shown to dominate wake development. Another common and more detailed approach is to use Large-Eddy Simulation (LES), which only dissipates turbulent features smaller than the grid resolution, whilst it solves larger ones. This produces detailed information about flow unsteadiness, turbulence and large scale vortices. It has also been used to study tidal turbines, but limited to few devices due to its larger computational expense (Creech et al., 2017; Blackmore et al., 2014; Afgan et al., 2013; Lloyd et al., 2014; Kang et al., 2014; Chawdhary et al., 2017).

First proposed by Spalart et al. (1997), Detached-Eddy Simulation (DES) is a hybrid approach to CFD that saves computational resources by using RANS near wall boundaries, while using the more resource-consuming and detailed LES only in areas of interest that contain large flow structures. This method for calculating instantaneous flow fields has been widely discussed in previous papers, and has been employed to solve coherent-structure dynamics for a variety of turbulent flows in a wide range of Reynolds numbers (Spalart et al., 1997; Escauriaza & Sotiropoulos, 2011; Spalart, 2009; Paik et al., 2005, 2010). It has been able to accurately reproduce experimental observations of mean flows and turbulence statistics in complex geometries, validating its use for studying hydrodynamics in different scenarios.

The methodology we propose to analyze tidal turbine hydrodynamics is a coupling of DES for solving the flow field, with BEM to represent tidal turbines. We argue that using a detailed turbulence model like DES can provide essential insights into wake development and turbine performance, even if our turbine representation approach is a simplified one. Besides informing on the interaction between turbines and their surrounding flow, we intend to validate our model and understand its advantages and limitations. For this

we compare with three configurations that were studied experimentally by Stallard et al. (2013) and Thomson et al. (2011), and numerically by Ingram & Olivieri (2012). These arrays are a single turbine case, a two staggered rows configurations comprised of seven turbines and a ten turbine array of two aligned rows of five turbines each.

The paper is organized in the following fashion: Section 2 explains the models being used and the interaction between them, along with the variables used in the analysis. Section 3 presents the case study used for validation, together with the parameters used for our numerical application of it. Later, Section 4 shows the results obtained with the BEM-DES model to this study case and discusses the main findings. Finally, Section 5 states the concluding remarks and future work of the investigation.

2. METHODOLOGY

To study the hydrodynamic effects of tidal turbine arrays, we have coupled a DES flow solver with a turbine representation model based on BEM. The advantage of DES is its ability to represent the instantaneous flow field and turbulence, while BEM allows to incorporate the effect of multiple HATTs simultaneously. The coupling rationale is based on the work by Creech et al. (2015), with a turbine model derived from BEM, which calculates lift and drag forces from tabulated airfoil data, and applies them as momentum sink terms to the incompressible Navier-Stokes equations. The computational solver uses non-staggered and structured grids, with generalized non-orthogonal curvilinear coordinates. Grids have higher resolution near cylindrical regions that represent the turbines. Every turbine is represented by a volume V , which is defined by the coordinates of its origin (x_T, y_T, z_T) , its radius R and its cylindrical length L , as shown in Figure 2.1.

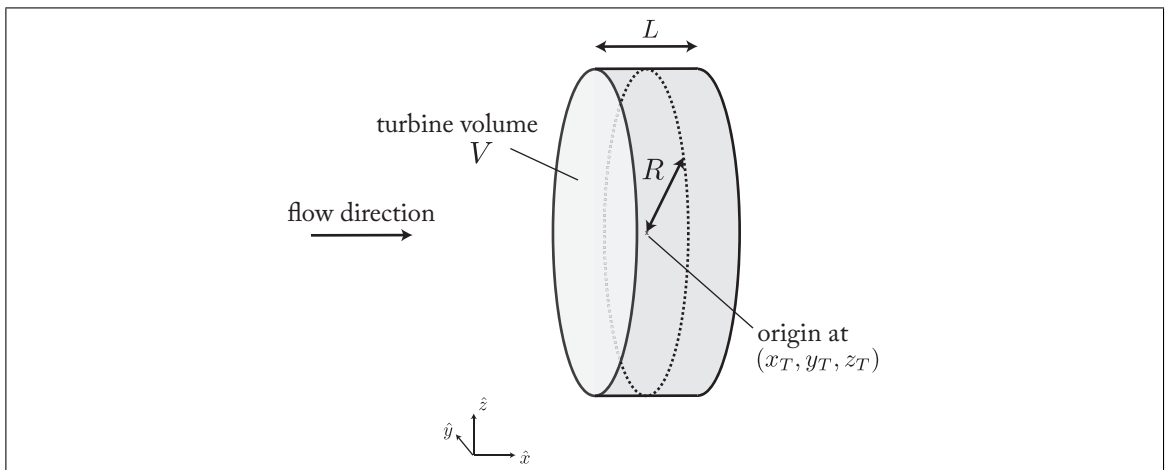


Figure 2.1. Schematic view of the cylindrical turbine volume V , with radius R and length L . Mesh nodes inside it are used for calculating the body forces that are passed to the Navier-Stokes equations in the DES model.

At the beginning of each simulation the code finds and stores the coordinates of every mesh node inside turbine volumes. It also stores the radial distance between the node and its respective turbine's center, the azimuthal angle between the node and the turbine center and the blade twist angle and chord length at the node's radial distance. These variables

and its use will be explained Section 2.2. Only in the grid points within turbine volumes body forces are calculated and passed into the Navier-Stokes solver.

As shown in Figure 2.2, for every time-step we obtain the local velocity field at every mesh node inside the turbine volume. If the node is outside the turbine hub, it calculates nodal lift and drag forces that are passed as body forces to the Navier-Stokes solver, and used to output performance and thrust measurements. If the node is inside the hub region, a zero velocity boundary condition is applied, in order to represent the drag induced on the flow by the structure. This assumption for the hub is a simplified way of considering velocity reduction at turbine hubs without solving their detailed geometry, and will be further discussed in Section 2.2.

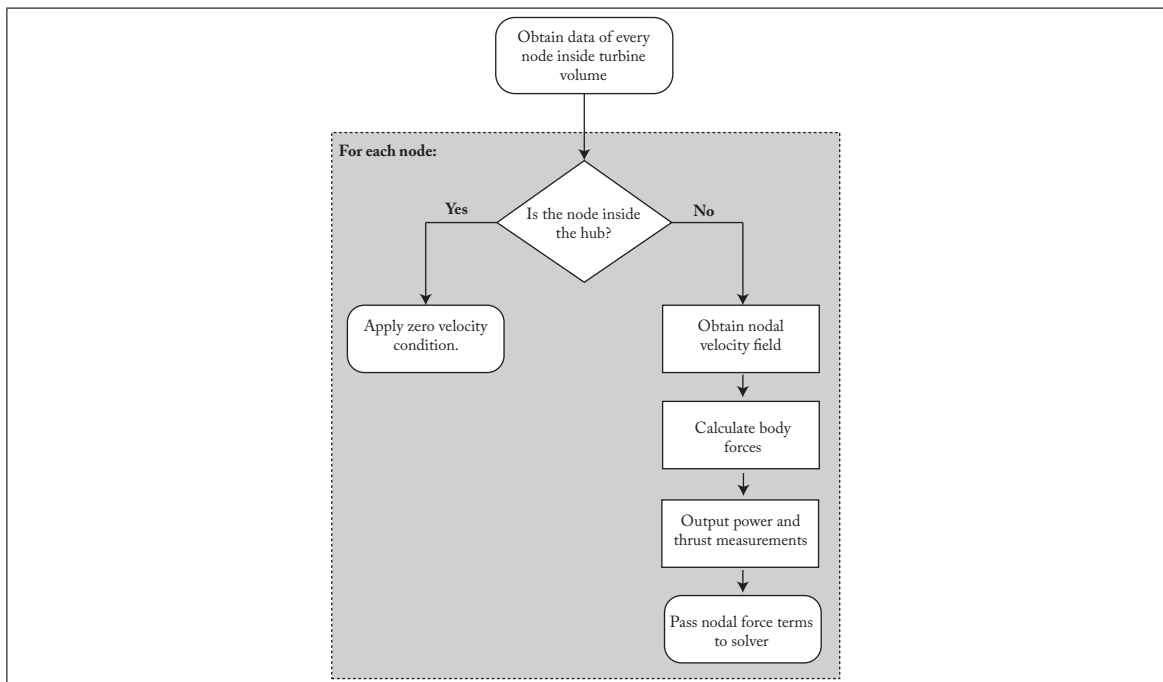


Figure 2.2. Overview of every time-step calculation procedure.

2.1. Detached-Eddy Simulation

In our simulations the governing equations are the incompressible, three-dimensional, unsteady, Reynolds-averaged Navier-Stokes equations for the conservation of mass and

momentum, solved with the method employed by Escauriaza & Sotiropoulos (2011). In tensor notation, these non-dimensionalized equations can be written as follows:

$$\frac{\partial \tilde{u}_i}{\partial \tilde{x}_i} = 0 \quad (2.1)$$

$$\frac{\partial \tilde{u}_i}{\partial \tilde{t}} + \tilde{u}_j \frac{\partial \tilde{u}_i}{\partial \tilde{x}_j} = -\frac{\partial \tilde{p}}{\partial \tilde{x}_i} + \frac{1}{Re} \frac{\partial^2 \tilde{u}_j}{\partial \tilde{x}_j \partial \tilde{x}_j} - \frac{\partial}{\partial \tilde{x}_j} \langle \tilde{u}'_i \tilde{u}'_j \rangle + \tilde{S}_i \quad (2.2)$$

where \tilde{S}_i is the momentum source (or sink) term, which is only considered in the nodes inside the turbine volumes. The length and velocity scales used for the nondimensionalization of the equations are the mean water depth \mathcal{H} and mean freestream velocity \mathcal{U} , respectively.

Here we highlight the model's main features and the reader is referred to the original paper for a detailed description of its application. It uses the hybrid formulation that combines URANS with LES (URANS/LES), first proposed by Spalart et al. (1997) and then revised in Spalart (2009). For the turbulence representation it uses a one-equation eddy-viscosity model developed by Spalart & Allmaras (1994).

It has been demonstrated that this method is capable of representing instantaneous flow fields and solving coherent-structure dynamics for turbulent flows in a wide range of Reynolds numbers. Previous studies show its ability to predict experimental observations and flow hydrodynamics for complex geometries (Escauriaza & Sotiropoulos, 2011; Spalart et al., 1997; Spalart, 2009; Paik et al., 2005, 2010).

2.2. Blade Element Momentum

The underlying concepts that explain the motion of HATTs are similar to the ones of airplane wings. Pressure differences between both sides of an hydrofoil generate forces that act on the surface of the hydrofoil and on the fluid moving around it. It is practical to decompose these forces into two components - Lift and Drag - as shown in Figure 2.4. Lift force (F_L) acts perpendicular to the velocity faced by the hydrofoil, whereas Drag (F_D) acts on the same direction as the velocity.

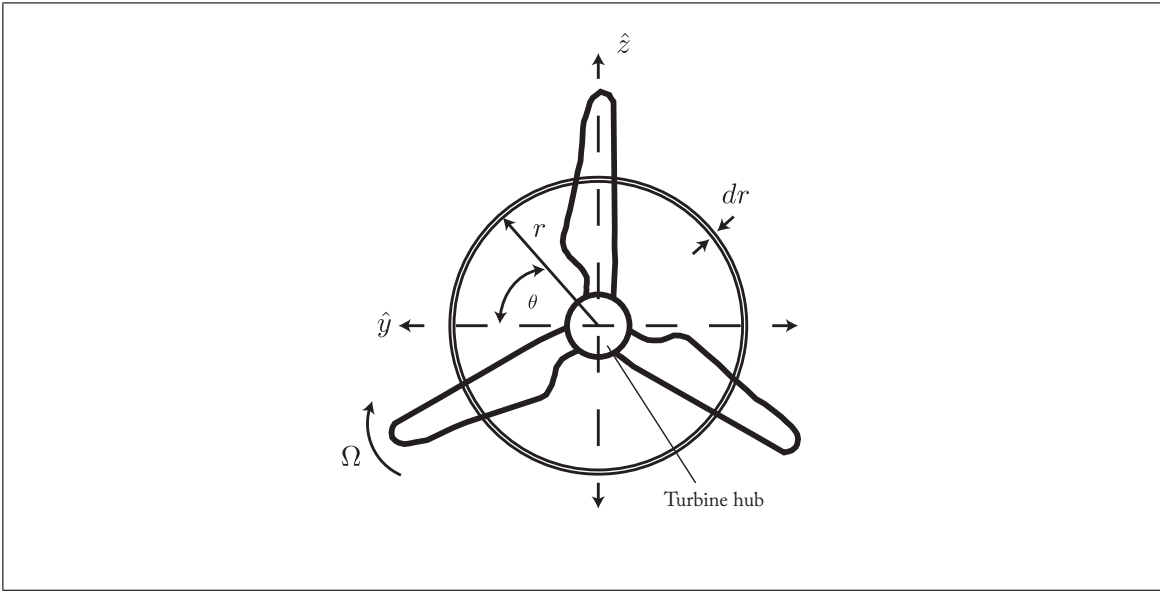


Figure 2.3. Frontal view of the variables used in Blade Element Momentum.

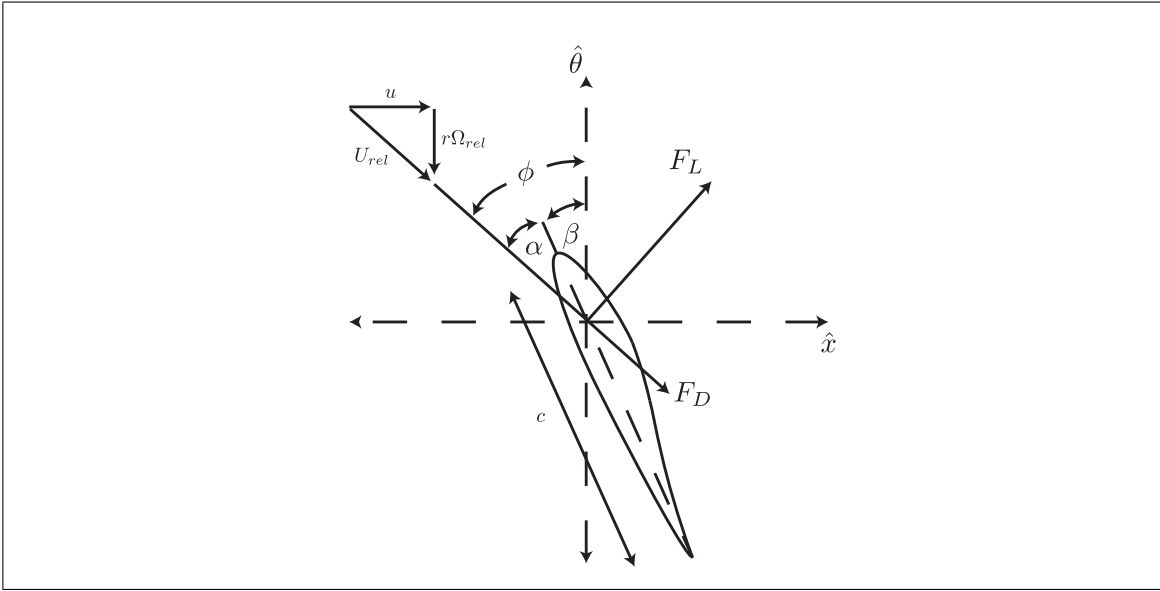


Figure 2.4. Blade section view of the variables involved in the lift and drag decomposition of Blade Element Momentum.

To incorporate blade effects onto the fluid we used a model based in a BEM application developed by Creech et al. (2015). Following the approach mentioned there, lift and drag

forces per span unit length on the blades can be described as follows:

$$f_L = \frac{1}{2} \rho c(r) U_{rel}^2 C_L(\alpha, Re) \quad (2.3)$$

$$f_D = \frac{1}{2} \rho c(r) U_{rel}^2 C_D(\alpha, Re) \quad (2.4)$$

where ρ is fluid density, U_{rel} is the relative speed between the blades and the fluid and $c(r)$ is the chord length of the blade at a radial distance r from the rotor center. C_L and C_D are the coefficients of Lift and Drag, respectively, and they are functions of airfoil geometry, the angle of attack α , and the Reynolds number Re of the fluid over the blade. In order to use these coefficients we use tabulated data that contains their value for different angles of attack and Reynolds numbers.

For a mesh node inside V , and located at a radial distance r from the disk center, relative speed U_{rel} is calculated as:

$$U_{rel} = \sqrt{u^2 + (r\Omega_{rel})^2} \quad (2.5)$$

where u is the local instantaneous longitudinal velocity component and Ω_{rel} is the relative rotational speed between the blade and the fluid. The latter is written as:

$$\Omega_{rel} = r\Omega + v \sin(\theta) - w \cos(\theta) \quad (2.6)$$

where θ is the azimuthal angle between the mesh node and the horizontal plane as shown in Figure 2.3, v and w are the local transverse and vertical velocity components, respectively, and Ω is the turbine rotational speed. This approach implies that both the rotation of the blades and the fluid are being considered in the calculations. For our application, turbine rotational velocity was considered to be fixed and a function of the turbine Tip Speed Ratio, $\lambda = R\Omega/U_\infty$. The relative flow angle ϕ , shown in Figure 2.4, can be obtained by

$$\phi = \tan^{-1} \left(\frac{u}{r\Omega_{rel}} \right) \quad (2.7)$$

With this, the local angle of attack is given by the following expression:

$$\alpha(r) = \phi - \beta(r) \quad (2.8)$$

where β is the local twist angle, defined as the angle variation of the blade from its position at the blade root. This angle is a function of r and depends on turbine blade design. Our model does not consider a dynamic blade pitch control, therefore β remains constant at every radial distance during the simulations.

In order to incorporate forces per unit length into the Navier-Stokes equations they must be transformed into body forces (forces per unit of volume), Creech et al. (2015) propose using

$$F_L = \eta(x^*) \left(\frac{N_{blades}}{2\pi r} \right) f_L \quad (2.9)$$

$$F_D = \eta(x^*) \left(\frac{N_{blades}}{2\pi r} \right) f_D \quad (2.10)$$

where N_{blades} is the number of blades and $\eta(x^*)$ is a Gaussian regularization function used to distribute the forces axially inside the turbine volumes. This regularization function smears out the influence of the blades only axially, since the azimuthal spreading of the forces is handled by the BEM approach with the second term in the equations above. Following Creech et al. (2015), the function $\eta(x^*)$ depends on the longitudinal distance between the mesh node and the disk center, $x^* = x - x_T$, and is defined as:

$$\eta(x^*) = \frac{1}{\sqrt{2\pi\sigma^2}} e^{-\frac{1}{2}\left(\frac{x^*}{\sigma}\right)^2} \quad (2.11)$$

where the standard deviation σ controls the width of the Gaussian filter. It has been shown that using $\sigma = \frac{1}{2}L$, where L is the length of the turbine volume, gives accurate prediction of turbine performance while controlling the need for excessively high mesh resolutions inside the turbine volumes (Creech et al., 2015).

Lift and drag forces are then decomposed into axial and azimuthal components acting on the fluid. Following Newton's third law, this forces are in the opposite direction to the

forces acting on the blade.

$$F_x = - (F_L \cos(\phi) + F_D \sin(\phi)) \quad (2.12)$$

$$F_{azim} = - (F_L \sin(\phi) - F_D \cos(\phi)) \quad (2.13)$$

The azimuthal component is then written in terms of its lateral and vertical directions

$$F_y = - \sin(\theta) F_{azim} \quad (2.14)$$

$$F_z = \cos(\theta) F_{azim} \quad (2.15)$$

Finally, the cartesian components of these forces are non-dimensionalized and passed to the DES solver where they are applied as source terms within the incompressible 3D momentum equations.

Since BEM only deals with the section of the turbine that is swept by the blades, when using actuator disks one must decide what to do in the turbine hub region, the nacelle and the support structure. In our model neither the nacelle nor the support structure were considered. Regarding the hub region, one option is not to apply any body forces in the area, but this has shown to make the hub zone act as a duct, accelerating the flow in it, and therefore negatively affecting overall turbine representation (Kang et al., 2014). Another approach is to consider the hub geometry as a solid and build a mesh around it, as it was done in Edmunds et al. (2017), Masters et al. (2013) and Malki et al. (2013). This gives better representation of the downstream wake but increases meshing complexity and needs an accurate depiction of turbine hub geometry. For our study, since we aim to study large turbine arrays we use a simplified approach to have velocity reduction in the hub, without the need to represent every turbine hub geometry: on every mesh node whose radial distance r is smaller than the hub's radius, we apply a zero velocity condition on every cartesian direction. It is important to ponder this simplification when analyzing the results, but as shown in Section 3, it gives valid results for wake development when comparing with experimental data.

2.3. Unsteady inlet

The presence of ambient turbulence can alter wake development and device performance, because fluctuations in the velocity field change wake mixing processes and local lift and drag characteristics in turbine blades. Previous investigations Lloyd et al. (2014), Blackmore et al. (2014) and Maganga et al. (2009) demonstrate these effects of inflow turbulence on HATTs, and stress the need to consider the issue when modelling devices and studying wake hydrodynamics.

As discussed by Tabor & Baba-Ahmadi (2010), there are myriad ways to incorporate inlet conditions for our type of simulations, which are generally collected into two categories: precursor simulation methods and synthesised turbulence methods. Precursor simulations basically consist of performing a separated detailed simulation to generate a database of inlet conditions that can be introduced into the main computation. Even though this approach produces realistic turbulent data, it can involve storing large amounts of data and is unwieldy to modify in order to match desired characteristics. Synthetised methods are based on producing syntethic inlet information constrained to desired variables, and are characterised by their ease of modification, which is the main reason we have chosen them for generating an unsteady inlet in our investigation.

Particularly, we have chosen a synthesised method called Random Flow Generation (RFG) developed by Smirnov et al. (2001). The RFG method produces an unsteady turbulent inflow that satisfies the conditions of continuity and correctly approximates anisotropy in turbulent flows, while being simple to modify in case different scenarios wished to be represented. Using a fully-developed URANS mean flow profile as a starting point, we apply RFG to obtain an inflow boundary condition that respects previously defined Reynolds stresses (i.e. velocity fluctuation correlations), and the length and time scales of the fluctuations that we wish to simulate. For detailed information on this procedure the reader is referred to Appendix A.

2.4. Analysis variables

2.4.1. Velocity field

To illustrate longitudinal momentum extraction we use the mean longitudinal component of velocity $\langle u \rangle$, and mean velocity deficit U_{def} . The latter is defined as

$$U_{def} = 1 - \frac{\langle u \rangle}{U_{hub}} \quad (2.16)$$

where U_{hub} is the mean velocity at the inlet and at hub height.

To study the rotational characteristics of turbine wakes we use the mean transverse and vertical components of velocity, $\langle v \rangle$ and $\langle w \rangle$ respectively. Also, we analyze mean axial vorticity $\langle \omega_x \rangle$, defined as:

$$\langle \omega_x \rangle = \frac{\partial \langle w \rangle}{\partial y} - \frac{\partial \langle v \rangle}{\partial z} \quad (2.17)$$

2.4.2. Turbulence statistics

For analyzing turbulence features we use Turbulent Kinetic Energy (TKE), k , defined as the mean kinetic energy contained in the turbulent velocity fluctuations u' , v' and w' :

$$k = \frac{1}{2} (\langle u'^2 \rangle + \langle v'^2 \rangle + \langle w'^2 \rangle) \quad (2.18)$$

It is also of interest to study Reynolds shear stresses $\langle u_i u_j \rangle$, the off-diagonal components of the Reynolds stress tensor. Zones in which these stresses are considerable are regions of increased turbulent mixing, characterized by high velocity gradients and where the effects of turbulent fluctuations on the mean flow increases.

2.4.3. Vortex visualization

Large scale vortices are visualized by using q -isosurfaces, first proposed by Hunt et al. (1988). Following their definition, a vortex is defined as the region where

$$q = \frac{1}{2} (\|\bar{\Omega}\|^2 - \|\bar{S}\|^2) > 0 \quad (2.19)$$

where Ω is known as the vorticity tensor and S is the rate-of-strain tensor, both derived from the velocity gradient tensor. This implies that vortices are defined as areas of the flow where the vorticity magnitude is greater than the rate-of-strain magnitude.

2.4.4. Bed shear stress

As discussed in Hill et al. (2014) and Hill et al. (2016), HATTs interact with the bed and alter sediment erosion and deposition processes. A way of evaluating this is through the shear velocity, which is a parametrization of the shear stress at the bed, and is defined as:

$$u_* = \sqrt{\frac{\tau}{\rho}} \quad (2.20)$$

where τ is the bed shear stress. From our simulations we obtain instantaneous snapshots of u_* and also time averaged values, allowing us to analyze possible zones of induced erosion or deposition of sediment because of the presence of HATTs.

2.4.5. Power and thrust coefficients

To analyze turbine dynamics it is common to use the power coefficient C_P and thrust coefficient C_T as indicators for comparison between devices. The power coefficient is defined as the ratio between the power extracted by the turbine blades and the maximum theoretical available power in the incoming flow. We use the following representation:

$$C_P = \frac{P}{0.5\rho U_\infty^3 A_d} \quad (2.21)$$

where A_d is the frontal area swept by the blades, U_∞ is the freestream velocity upstream of the devices, and power P is obtained by integrating the contribution of every node inside the turbine volume:

$$P = \int_V \Omega (r F_{azim}) dV \quad (2.22)$$

The thrust coefficient is defined as the ratio between the axial force acting upon the turbine and the kinetic energy in the incoming flow. We represent this as:

$$C_T = \frac{T}{0.5 \rho U_\infty^2 A_d} \quad (2.23)$$

where the total thrust on the turbine, T , is obtained similarly to P , with:

$$T = \int_V F_x dV \quad (2.24)$$

3. PERAWAT CASE STUDY

In this study we use our DES-BEM model to compare with some of the turbine arrays analyzed as part of the Performance of Arrays of Wave and Tidal (PerAWaT) project, commissioned by the Energy Technologies Institute (ETI) ¹. This is done by contrasting our results with the experimental work done by Stallard et al. (2013) and Thomson et al. (2011), and with the numerical simulations based on the experiments done by Ingram & Olivieri (2012). They used a BEM-URANS model and considered both the turbine nacelle and hub geometry.

3.1. Flume and turbine geometry

Experimental tests were carried out in the University of Manchester wide flume, which has a width of $5m$ and a test section $12m$ long. The tests were performed with a characteristic water depth of $0.45m$ and a mean freestream velocity of $0.45m/s$, which results in a flume Reynolds number of 202,500. The inlet has a porous weir to produce ambient turbulence intensity of approximately 10% (Stallard et al., 2013). In the computational domain a rectangular mesh was used to represent the full width and height of the flume. In the streamwise direction the mesh extends $5D$ upstream from the first row of devices and $30D$ downstream from it. Details about the used meshes will be presented in Section 3.3.

In every array configuration identical rotors were used. Each of them has three blades with a Göttingen 804 foil geometry and radial chord length and twist variation. Blades were designed to give similar thrust coefficient variation with tip speed ratio in comparison with a generic full-scale turbine (Stallard et al., 2013). Key turbine parameters are summarized in Table 3.1. Because of the increase of meshing complexity and computational cost it would imply, neither the nacelle nor its support structure were considered in our computational simulations.

¹For more information visit <http://www.eti.co.uk/programmes/marine/perawat>

Table 3.1. Principal turbine parameters for the studied test case.

Symbol	Definition	Value	Unit
D	Turbine diameter	0.27	m
D_h	Hub Diameter	0.03	m
N_b	Number of blades	3	—
U_∞	Mean freestream velocity	0.45	ms^{-1}
Ω	Turbine rotational velocity	15	s^{-1}
λ	Tip speed ratio	4.5	—

3.2. Arrays studied

We compare three array configurations studied in Stallard et al. (2013). Our starting point is the single turbine array, then we analyze a seven turbine array comprised of two staggered rows separated by 4 diameters, and finally we model a ten turbine array with two aligned rows of five turbines each with 8 diameters of longitudinal separation. In every case, the central turbine of the first row is located at the center of the flume, vertically and laterally. Arrays are illustrated in Figure 3.1. The figures are not to scale, so devices seem much closer to flume walls than in the actual experiments, where turbines are far from them and can be considered to be operating without the influence of the flume’s lateral boundaries.

3.3. Grids

Rectangular grids were used for every simulation. In each one of them the number of nodes, the spacing in the near-rotor region of every turbine volume and the turbine volume cylindrical length were the same, with the values shown in Table 3.2. Mesh resolution increases near the location of the turbine volumes, as illustrated in Figure 3.2 for the two staggered rows case. In the longitudinal direction every turbine volume has five node slices, but vertically and laterally the number of nodes changes because of different mesh stretching conditions at different array configurations. The maximum and minimum number of nodes inside every volume is presented in Table 3.3. Regarding mesh sensitivity, we argue that the used resolution is sufficient for capturing the fundamental physical

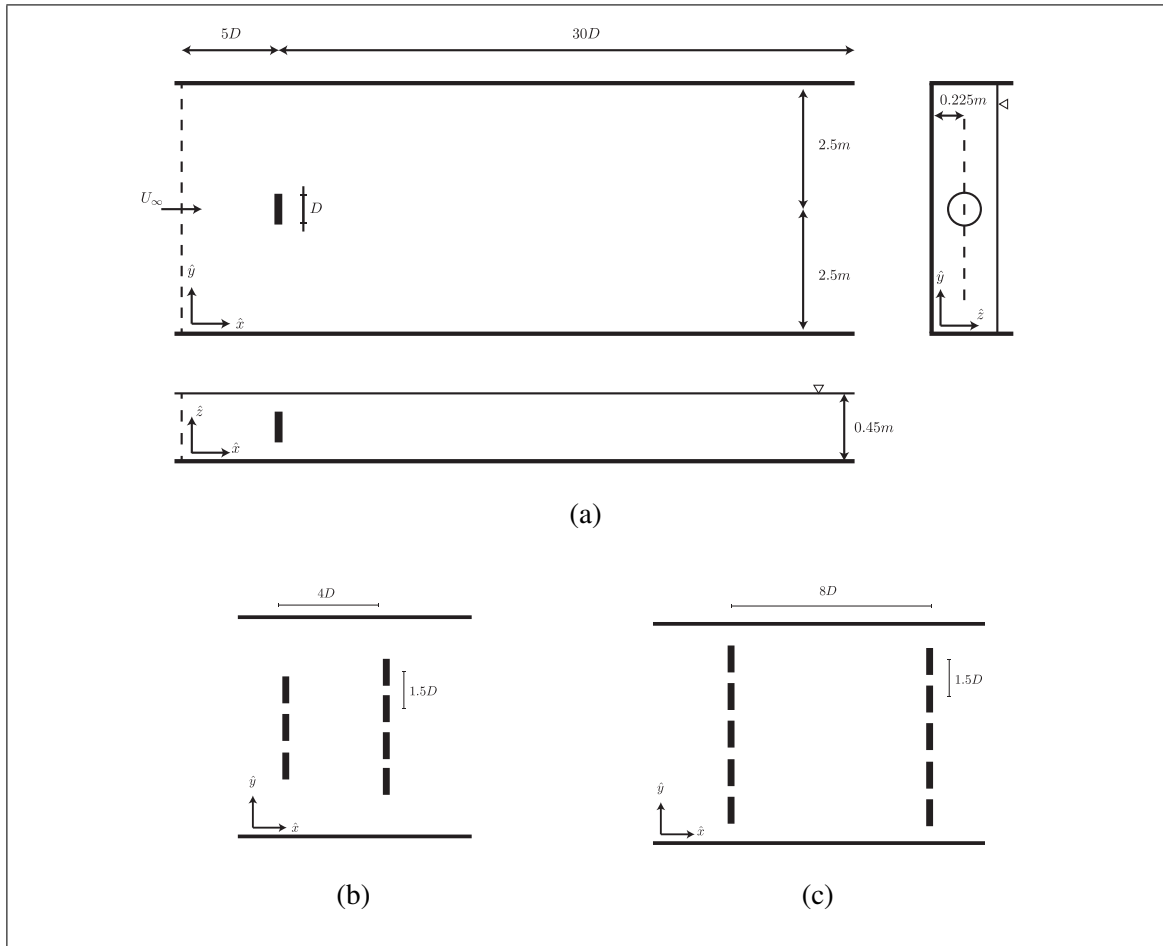


Figure 3.1. Schematic representation of (a) single turbine case; (b) two staggered rows array and (c) two aligned rows array. Like in the single turbine case, the central turbine of the first row in (b) and (c) is located at the vertical and lateral center of the flume, and at a distance of $5D$ downstream from the inlet. Lateral spacing between devices is the same in every array. The figures are not to scale, so devices seem much closer to flume walls than in the actual experiments, where turbines are far from them and can be considered to be operating without the influence of the flume's lateral boundaries.

phenomena associated with tidal turbines, with grids that have greater refinement than reported models that require more complexity, like the ALMs and solved geometry approaches done by Kang et al. (2014) and Chawdhary et al. (2017). This is supported with the obtained results that will be presented in Section 4.

Table 3.2. Details of the parameters used for the computational meshes. N_i and Δi indicate the number of nodes and spacing in the i direction, respectively. (L/D) represents the cylindrical length of the turbine volumes with respect to turbine diameter.

$N_x \times N_y \times N_z$	$282 \times 361 \times 101$
Number of nodes	10,282,002
Near-rotor $\Delta x/D$	10^{-2}
Near-rotor $\Delta y/D$	8.3×10^{-3}
Near-rotor $\Delta z/D$	8.3×10^{-3}
Turbine volume (L/D)	4%

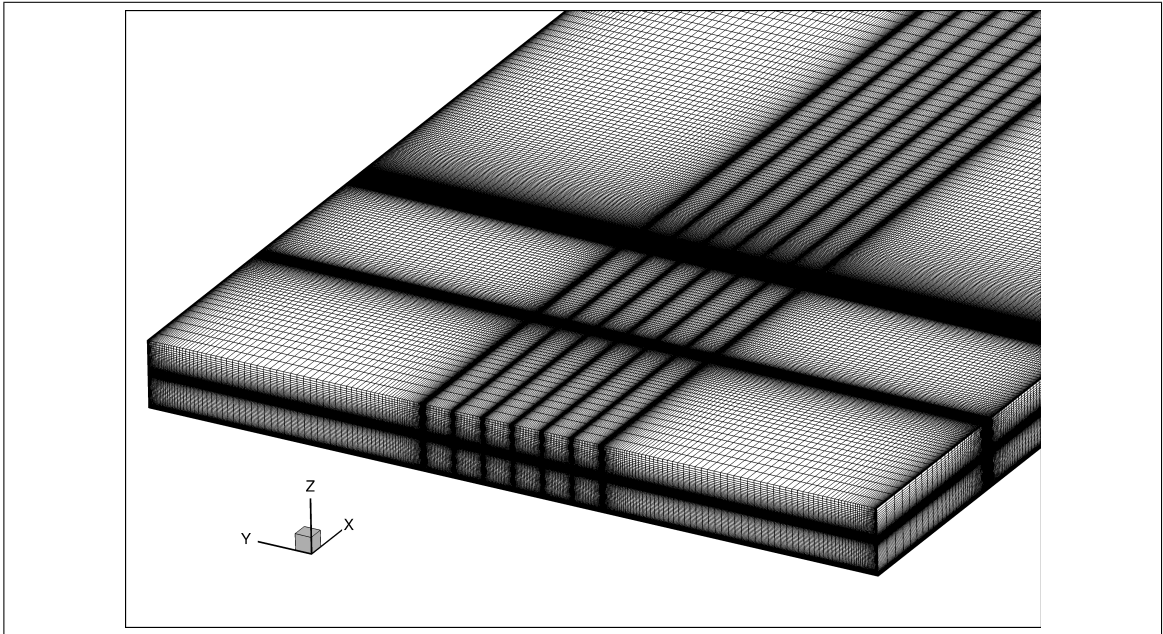


Figure 3.2. Grid used for the two staggered row case.

Table 3.3. Minimum and maximum number of nodes inside the turbine volumes for every studied array.

Array	Min. number of nodes inside turbine volume	Max. number of nodes inside turbine volume
Single turbine	14,560	—
Two staggered rows	8,355	9,155
Two aligned rows	6,865	9,230

3.4. Boundary conditions

All the cases presented in this study have an inlet boundary condition that uses an unsteady flow generator, as described in Section 2.3. At the outflow boundary, a zero gradient boundary condition is applied. At the flume's bed we use a no-slip boundary condition, with a mesh resolution fine enough to resolve the viscous sub-layer in this region. In the lateral walls of the flume, we use wall functions (Kalitzin et al., 2005) in order to decrease the number of nodes needed in that zone. Finally, even though free-surface effects have been shown to influence tidal turbine operation and wake development (Hill et al., 2014; Riglin et al., 2015), it is beyond the scope of this study to incorporate them, and consequently a flat and rigid slip wall with a symmetry boundary condition is used in the top surface of the domain.

4. RESULTS

In this section we first present and discuss the results for the single turbine case. Thereafter, we present the results obtained for the staggered and aligned rows cases, comparing and contrasting the obtained flow fields, wake structures and performance measurements. To analyze the mean flow we time averaged the flow field for the equivalent to 450 turbine revolutions in the single turbine case, and for 200 device revolutions for both double row arrays. This allows us to capture rich hydrodynamics features of fully developed tidal turbine wakes. Unfortunately not always both numerical and experimental information were available for comparing, but when possible the analysis is made using both.

4.1. Single turbine

4.1.1. Mean flow field

We observe than in the near wake region of the single turbine case there is a difference in velocity deficit distribution when comparing to experimental results. This near wake difference is illustrated in Figure 4.1a, and is characteristic of BEM approaches which are known to be unable to correctly reproduce near wake effects (Masters et al., 2015; Creech & Früh, 2016). Our simplification of not considering the turbine nacelle and support structure geometry also contribute to this disagreement in the near wake region. The difference diminishes downstream of the turbine, and in the far wake the agreement with experimental observations improves. The axial velocity profile shown in Figure 4.1b demonstrates this improvement, but still indicates that the simulated velocity distribution along the hub axis tends to be underestimated in the order of 10%, with a similar rate of recovery than the experimental results. This is indicated by the same slope of both curves in the far wake region.

To further look into wake characteristics after a single device we plot in Figure 4.2 contour plots of mean flow variables. The mean longitudinal velocity $\langle u \rangle$ plot indicates momentum extraction and velocity reduction downstream of the turbine, followed by a

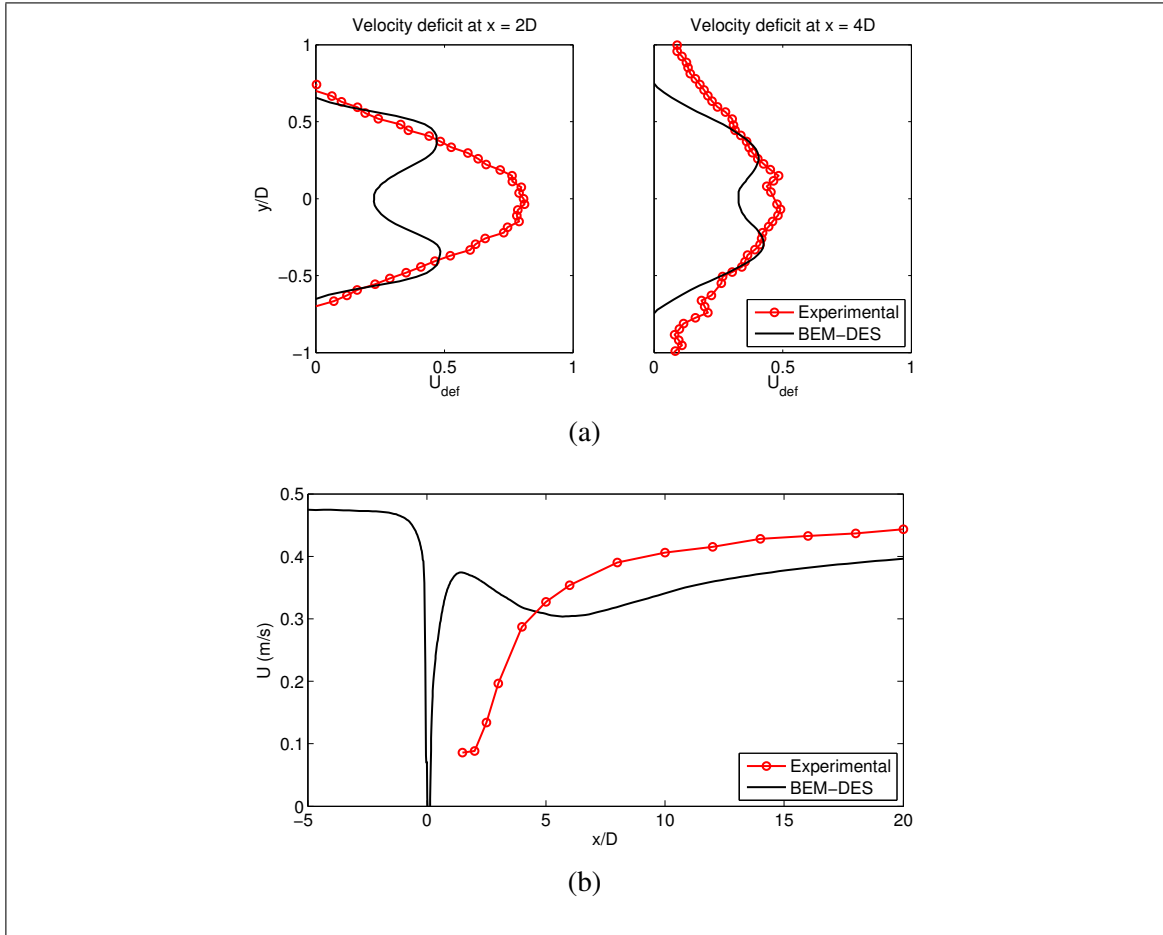


Figure 4.1. Lateral and longitudinal plots of axial velocity. (a) Lateral profiles of velocity deficit for the single turbine case. The difference between the curves is explained because of the limitations of BEM applications and our simplification of not simulating the complete hub, nacelle and support structure geometry; (b) Axial velocity profile along the hub axis for a single turbine. Velocity tends to be underestimated in approximately 10% by the DES-BEM model, but both curves show the same rate of recovery.

gradual recovery that lasts up to $20D$ downstream from it. Velocity reduction near the hub produces a reversed flow region immediately downstream from it. The mean transverse velocity $\langle v \rangle$ plot shows an internal zone where the wake rotates contrary to the turbine blades, and a region downstream of the hub with the same direction of rotation than the blades. These two counter-rotating regions can be better appreciated when plotting axial vorticity $\langle \omega_x \rangle$. Both Figures 4.2b and 4.2c show that the produced rotating zones remain

mainly columnar up to $5D$, after which rotation decreases and the wake expands radially. The Figures also indicate that BEM is able to reproduce rotational characteristics downstream of the blade region and that our hub approach generates a counter rotating vortex, but that our simulation is still not able to reproduce tip vortices, described in detail in the work done by Kang et al. (2014). These vortices are produced by local effects of turbine tips over the flow that are lost when the turbine effects are smeared over a disk, like in BEM.

When analyzing turbulence statistics depicted in Figure 4.3 it can be seen that there are two regions where turbulent fluctuations have a greater influence on the mean flow and on wake dynamics: the zone downstream of what would be the turbine tips ($z/D = \pm 0.5$), and downstream of the turbine hub. This is characteristic of regions of high velocity gradients, such as the outer region where the wake interacts with the faster moving ambient flow, and around the hub where velocity is zero. Pockets of high TKE coincide with the location of high principal Reynolds shear stress. As described in the work done by Kang et al. (2014), the pockets of high TKE and shear stress merge close to where turbine wake rotation diminishes. In our case this occurs around $5D$ downstream from the single device. In real turbines, turbine blades and tips also generate turbulence and instabilities due to local flow effects of separation and instability which are not present in our simulations due to the limitations of BEM. To address this, synthetic turbulence generation methods have been proposed, like the one used by Creech et al. (2015) for wind turbines, and could be considered in a further development of the methodology proposed in this study.

It is worth noting that on every plotted variable in Figures 4.2 and 4.3, the influence of the turbine can still be found up to $15D$ downstream of it, with mean longitudinal velocity still considerably reduced up to $20D$. Additionally, differences between the superior and inferior regions seen on the vertical planes shown above demonstrate an effect of the flume bed on wake development. The studied device occupies 60% of the water column, therefore bed effects can be considered important. This is evidenced in lower levels of TKE and

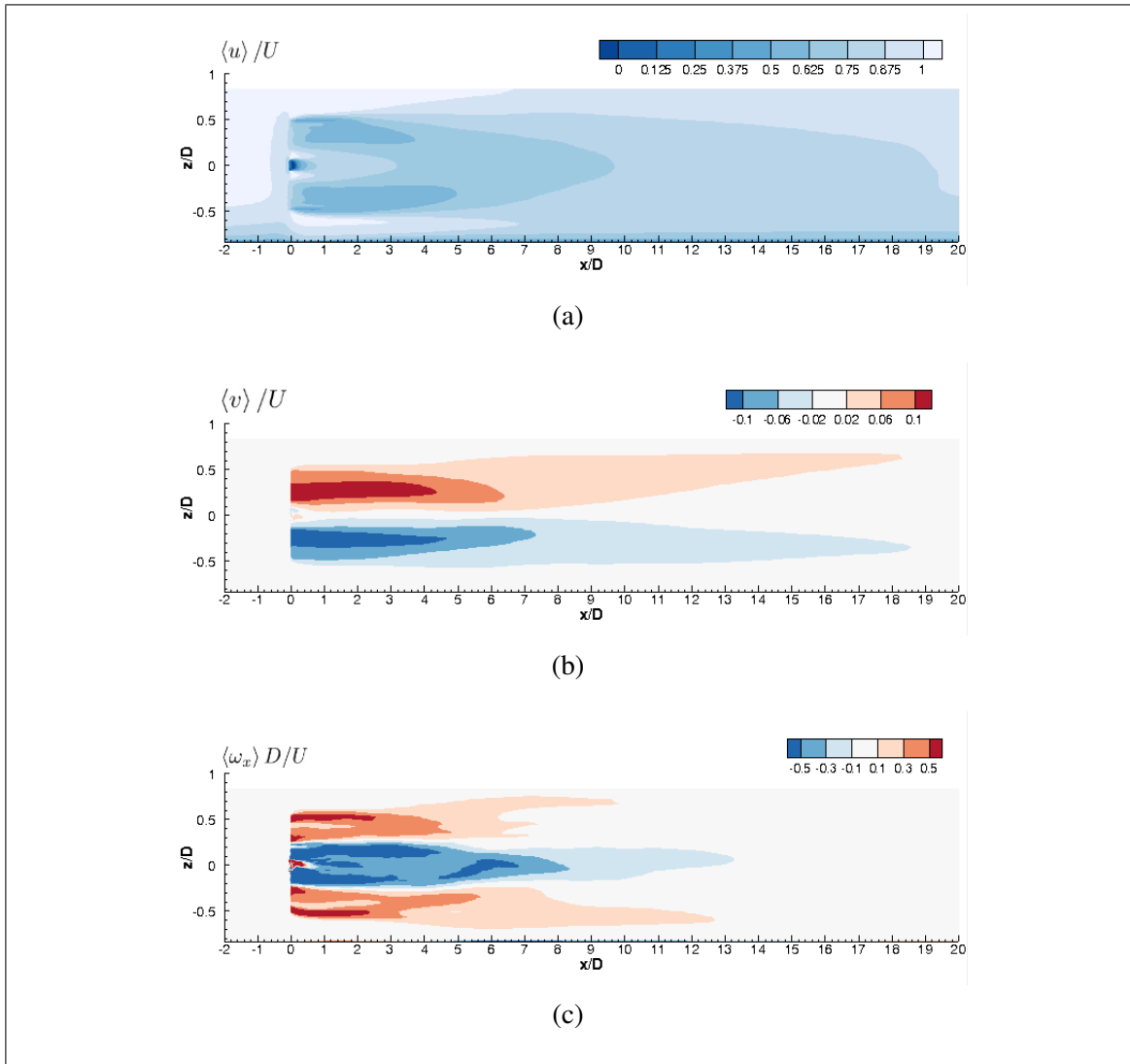


Figure 4.2. Contour plots of mean flow statistics at a vertical plane at $y/D=0$ for the single turbine case: (a) non-dimensional mean longitudinal velocity; (b) non-dimensional mean transverse velocity; (c) non-dimensional mean axial vorticity.

shear stress in the inferior section of the wake, where the proximity to the boundary produces fluctuations of lower intensity, and create a vertical assymetry in the development of the wake.

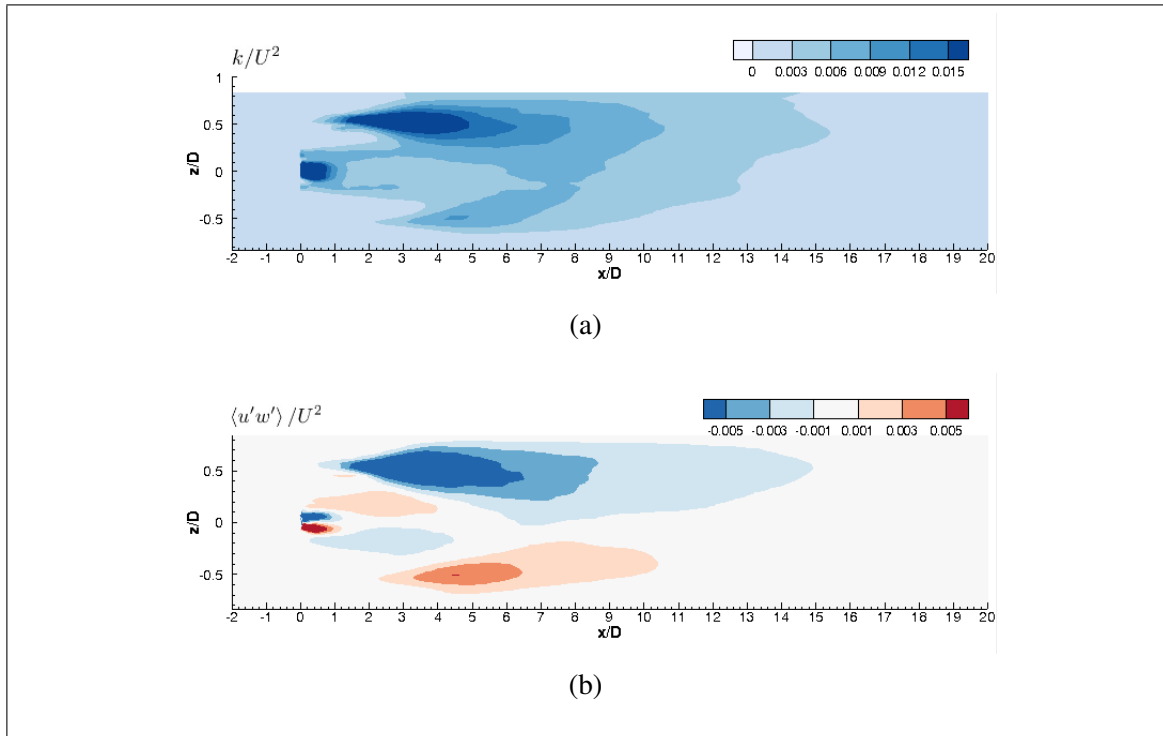


Figure 4.3. Contour plots of turbulence statistics at a vertical plane at $y/D=0$ for the single turbine case: (a) non-dimensional TKE; (b) non-dimensional principal Reynolds shear stress.

4.1.2. Instantaneous flow field

The q iso-surfaces shown in Figure 4.4 illustrate the effect our turbine model has on the instantaneous flow. First, even though BEM does not reproduce tip vortices, we still appreciate that the region surrounding our turbine is characterized by annular vortex shedding, in the length scale of the device diameter. Second, the hub produces a rotating vortex whose size is in the scale of the hub diameter. Both structures gradually expand radially, and eventually interact, losing coherence around $5D$. This is coincidental with the zones of increased turbulence statistics and decreased rotation in the wake.

The results presented above for the mean and instantaneous flow help understand the effects a single turbine has on its surrounding environment and how its wake develops. Besides, it shows the validity of our BEM-DES implementation to represent tidal turbines. Two counter-rotating regions were appreciated downstream of the device. They interact

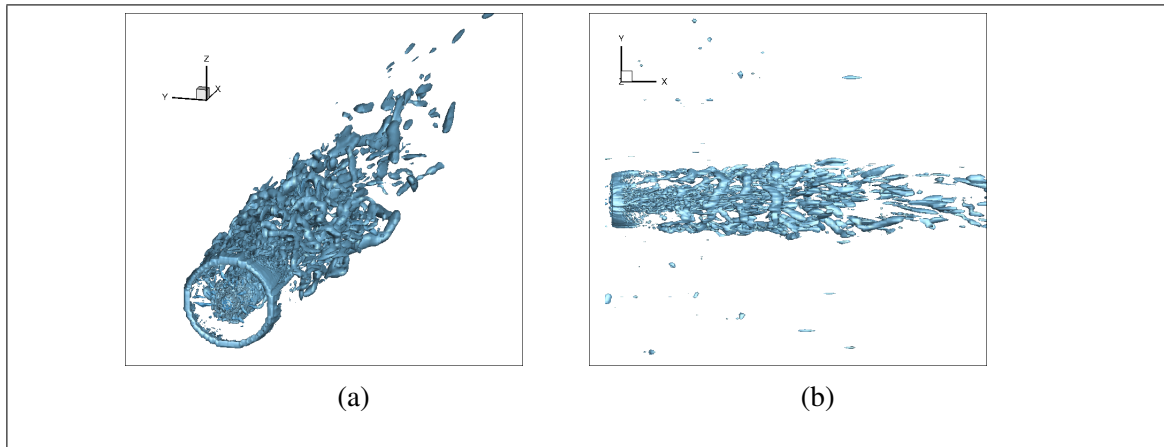


Figure 4.4. Plots of q iso-surfaces for the single turbine case. (a) three dimensional view; (b) superior view.

around $5D$ downstream from the turbine, where rotation is considerably reduced, and zones of high TKE and Reynolds shear stress merge. This was visualized with q iso-surfaces, that showed coherent structures produces around the tip region of the turbine and around the hub. These structures lose their coherence in the same region where rotation decreases and zones of high turbulence statistics interact.

This emphasizes the argument that even though BEM can be thought of as a simplified approach to represent tidal turbines, it can still provide fundamental insights into understanding wake hydrodynamics and the overall effect a device has on the ambient flow, both for the mean and the instantaneous flow field. As it will be discussed in the subsequent section, the approach remains specially beneficial when it is applied for arrays of multiple devices.

4.2. Arrays

4.2.1. Mean flow field

When analyzing mean velocity profiles for doubled row arrays the difference in the hub region of every turbine relative to the experiments is considerably improved downstream from the posterior row of devices, even in the near wake region. As shown in

Figures 4.5 and 4.6, our DES-BEM model gave better predictions for experimental data than URANS-BEM simulations done by Ingram & Olivieri (2012), even though the latter approach included both turbine hub and nacelle geometry into the simulations. This improvement was seen in both doubled row cases, and confirmed using Mean Square Error and Nash-Sutcliffe Coefficient for comparison (Bennett et al., 2013). Figure 4.6 depicts that the region where the disagreement with experiments is worse is the immediate proximity of the device, $x/D < 2$, after which the profiles match the experimental predictions. Considering these results, it could be argued that initial differences in wake prediction emerging from geometrical simplifications are dissipated by the large scale structures present in the flow incoming from upstream rows. The results indicate that these turbulent conditions make geometrical simplifications, like not considering the nacelle, apparently less relevant in order to predict mean velocity profiles for turbine arrays, and that using a more detailed turbulence model like DES contributes to improving mean flow field representation.

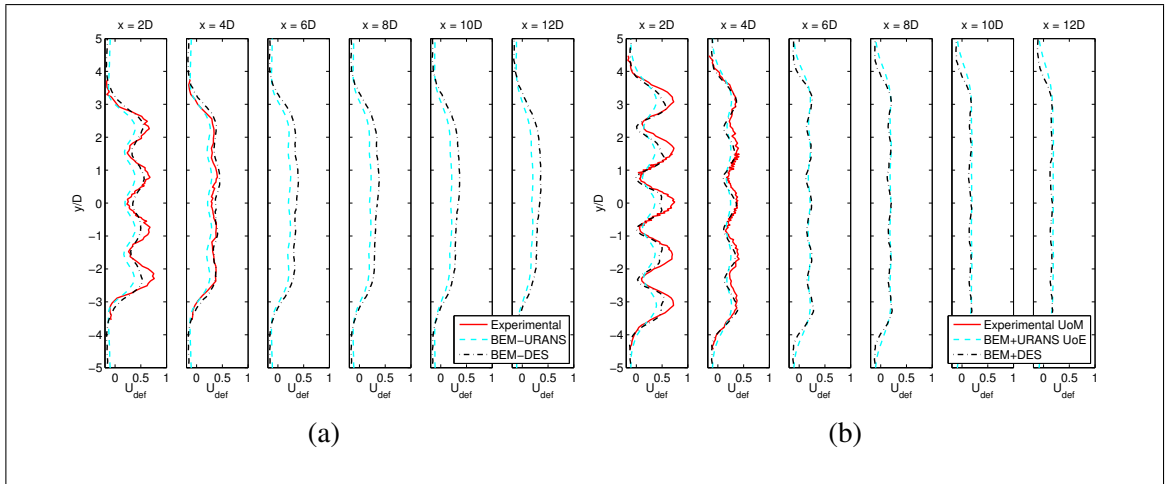


Figure 4.5. Lateral profiles of mean velocity deficit, with distance measured from the second row of turbines. (a) two staggered rows; (b) two aligned rows. The BEM-DES simulations show good agreement with the experimental data even in the near wake region, with predictions being better than the BEM-URANS application.

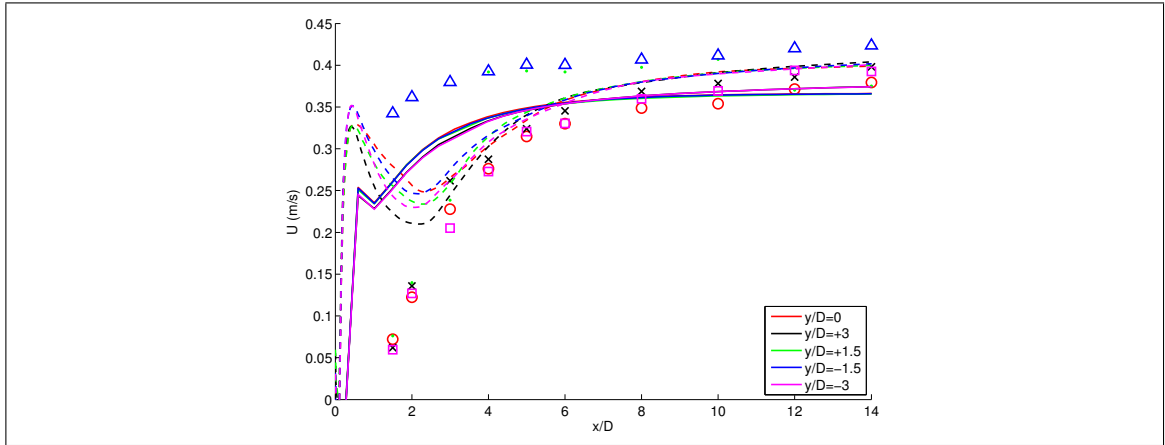


Figure 4.6. Axial profiles of mean longitudinal velocity downstream of the second row of the two aligned rows array, with velocity taken at hub height. Continuous lines represent BEM-URANS results, dashed lines are our DES-BEM results and isolated icons represent experimental results. After $2D$ downstream the DES-BEM improves the representation on profile evolution, matching the experimental data.

In addition, our simulations of turbine arrays showed that flow statistics vary considerably from the single turbine case when device wakes interact with each other and when turbines operate under the influence of upstream devices. As depicted in Figure 4.7 for the two staggered rows case, turbines in frontal rows have similar behavior as a single device, but this changes for posterior devices. In particular, as seen in Figure 4.7a, mean velocity deficit is higher downstream of posterior rows, and approximately $5D$ from the second row individual turbine wakes merge into a single array wake. One remarkable result is that rotation in the wake diminishes faster for posterior rows, like it is seen in Figures 4.7b and 4.7c. Rotation is considerably reduced around 3 diameters downstream of the devices, in contrast with the 5 diameters seen in the single turbine case. Arguably, the influence of upstream wakes contributes to destabilizing the wake of posterior devices faster, facilitating mixing between the wakes and the ambient flow, and accelerating wake development. These results were also seen for the aligned row case, with rotation diminishing near $x/D = 4$ downstream of the second row. Since both arrays have different longitudinal spacing between rows ($4D$ for the staggered case and $8D$ for the aligned one), posterior devices face upstream wakes at different stages of its development, with the aligned case

at a distance large enough for the upstream wakes to have recovered more than in the staggered case. This changes the evolution of posterior wakes, but unfortunately our studied cases do not allow us to separate the effect of row alignment and longitudinal spacing on this results.

The results for TKE and Reynolds shear stress also illustrate the difference between single devices and arrays, and confirm that posterior wakes are characterized by higher influence of turbulent fluctuations on the mean flow. This is depicted in Figure 4.8 for the aligned rows. It can be seen that both turbulence statistics increase for posterior devices, evidencing strong interaction among turbine wakes, and also between wakes and the ambient flow. Second, we appreciate that the high turbulence zones at the outer wake and in the hub region merge closer to the turbines with respect with the single device study, in congruence with faster rotation reduction discussed above. Additionally, even though in the central part of the array turbulence statistics tend to diminish gradually and become negligible around $8D$ from the second row, they remain significant in the outer boundaries of the wake ($y/D = \pm 3.5$ in Figure 4.8), indicating that the ambient flow and the array wake keep interacting in this zone. Results for the staggered rows case can be found in Appendix C.

4.2.2. Instantaneous flow field

Figure 4.9 depicts the visualization of q iso-surfaces for both double row arrays, showing the presence of vortical structures. This clarifies the higher complexity of the flow faced by devices in posterior rows. Additionally, downstream wakes have a larger presence of coherent structures, nevertheless, it is apparent from this Figure that vortical structures lose coherence faster than in the single device case, arguably because of the induced mixing of upstream wakes.

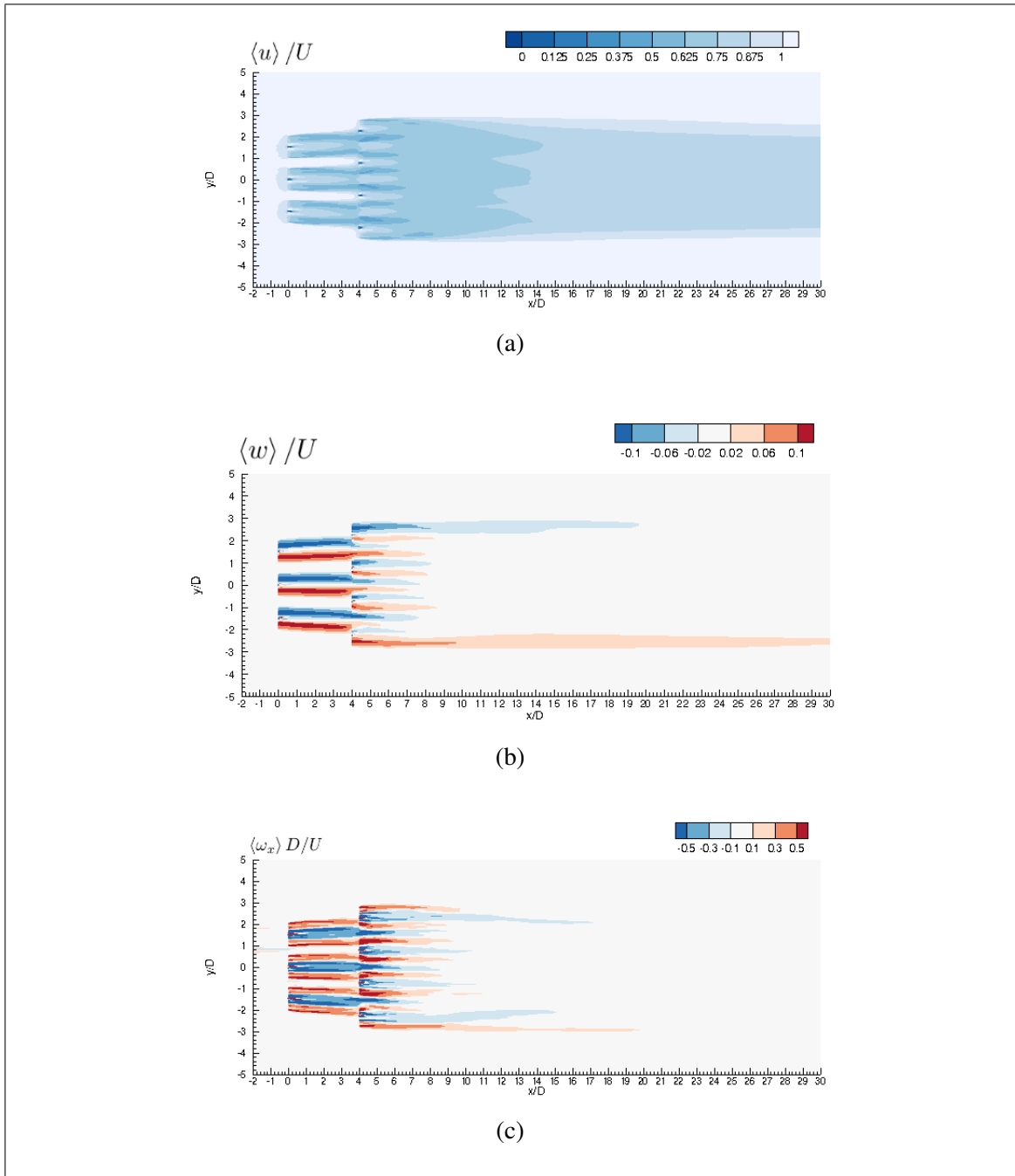


Figure 4.7. Contour plots of mean flow statistics at a horizontal plane at $z/D = 0$ for the two staggered rows case: (a) non-dimensional mean longitudinal velocity; (b) non-dimensional mean vertical velocity; (c) non-dimensional mean axial vorticity.

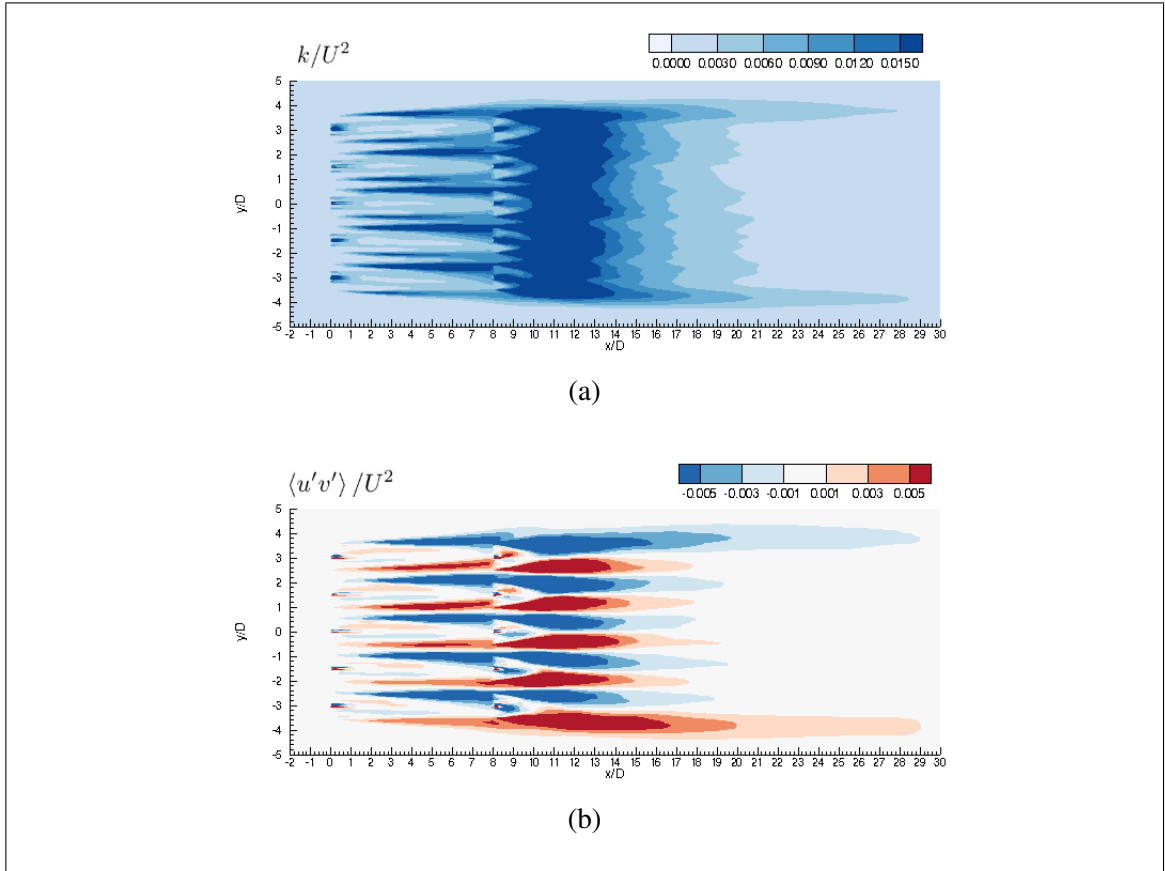


Figure 4.8. Contour plots of turbulence statistics at a vertical plane at $y/D=0$ for the single turbine case: (a) non-dimensional TKE; (b) non-dimensional principal Reynolds shear stress.

4.2.3. Effects on the bed

For shear velocity u_* , results show that regions of flow acceleration between turbines on the same row are characterized with higher levels of u_* , and therefore are more likely to be affected by scour. On the contrary, downstream of turbine centers, where velocity deficits are higher, u_* was smaller, and therefore they are a zones preferable for sediment deposition (see Figure 4.10a). This characteristics are in line with the experimental results obtained by Hill et al. (2014) and Hill et al. (2016), who studied bedform evolution and sediment transport with an experimental scale device. It is worth noting that even though mean values for u_* are similar for frontal and posterior rows, temporal evolution is not. This is illustrated in Figure 4.10b, that shows how the RMS of u_* can be up to five times

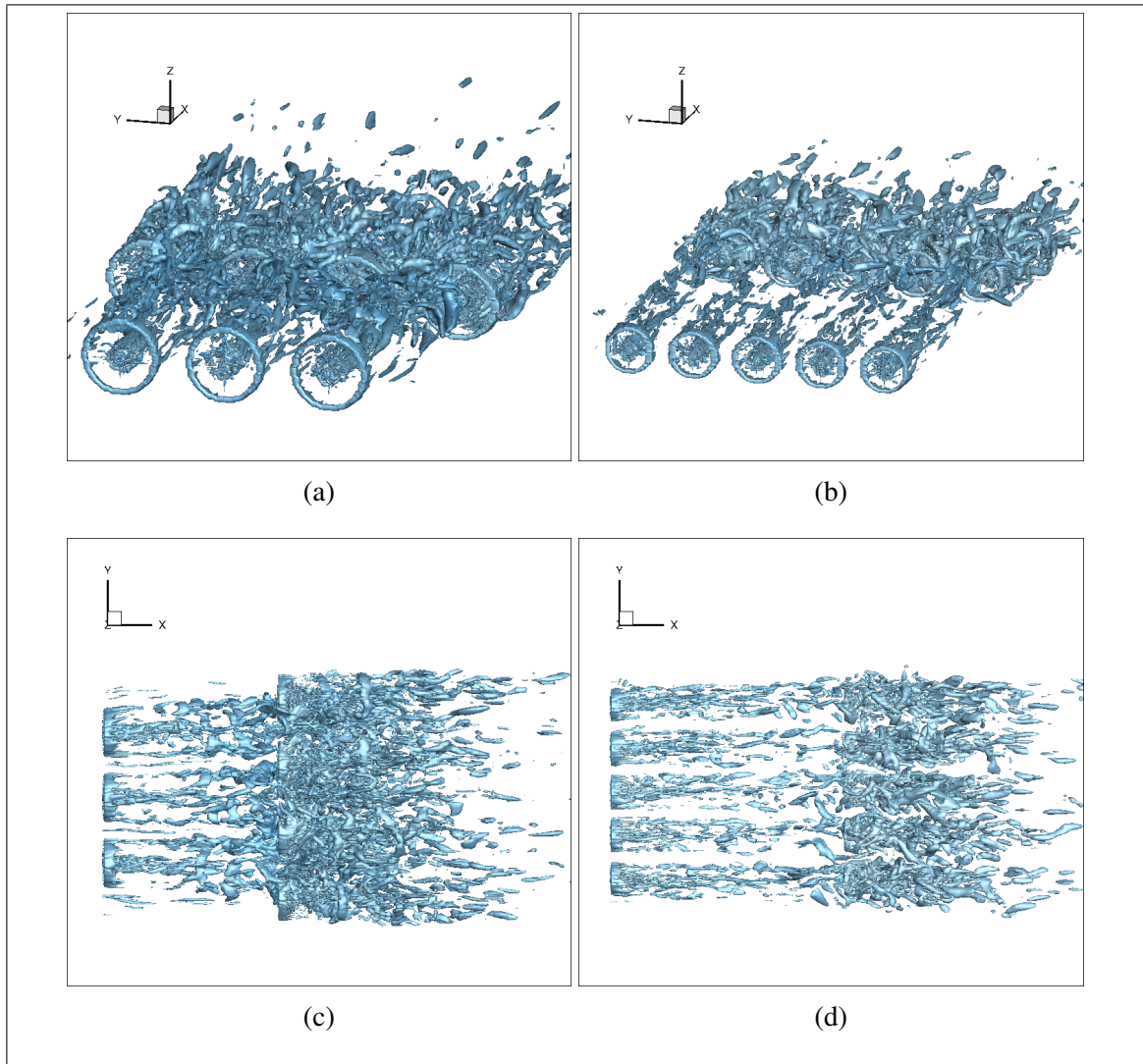


Figure 4.9. Plots of q -isosurfaces for the studied arrays. (a),(c): two staggered rows; (b),(d): two aligned rows.

higher in the posterior row of the aligned rows array, with a deviation in the order of 10% of the mean value. Similar results were appreciated for the staggered rows case. As discussed previously, the region downstream of the second row of devices is characterized by an increase in TKE and Reynolds shear stress, with a flow with higher presence of vortices and turbulent fluctuations, which causes u_* to have larger temporal fluctuations in this zone too. This raises the question if designing tidal turbines considering mean values is sufficient, or if these temporal fluctuations are important enough to be considered

in the device design and operation process. The obtained results for the influence of the staggered rows array on the bed can be found in Appendix D.

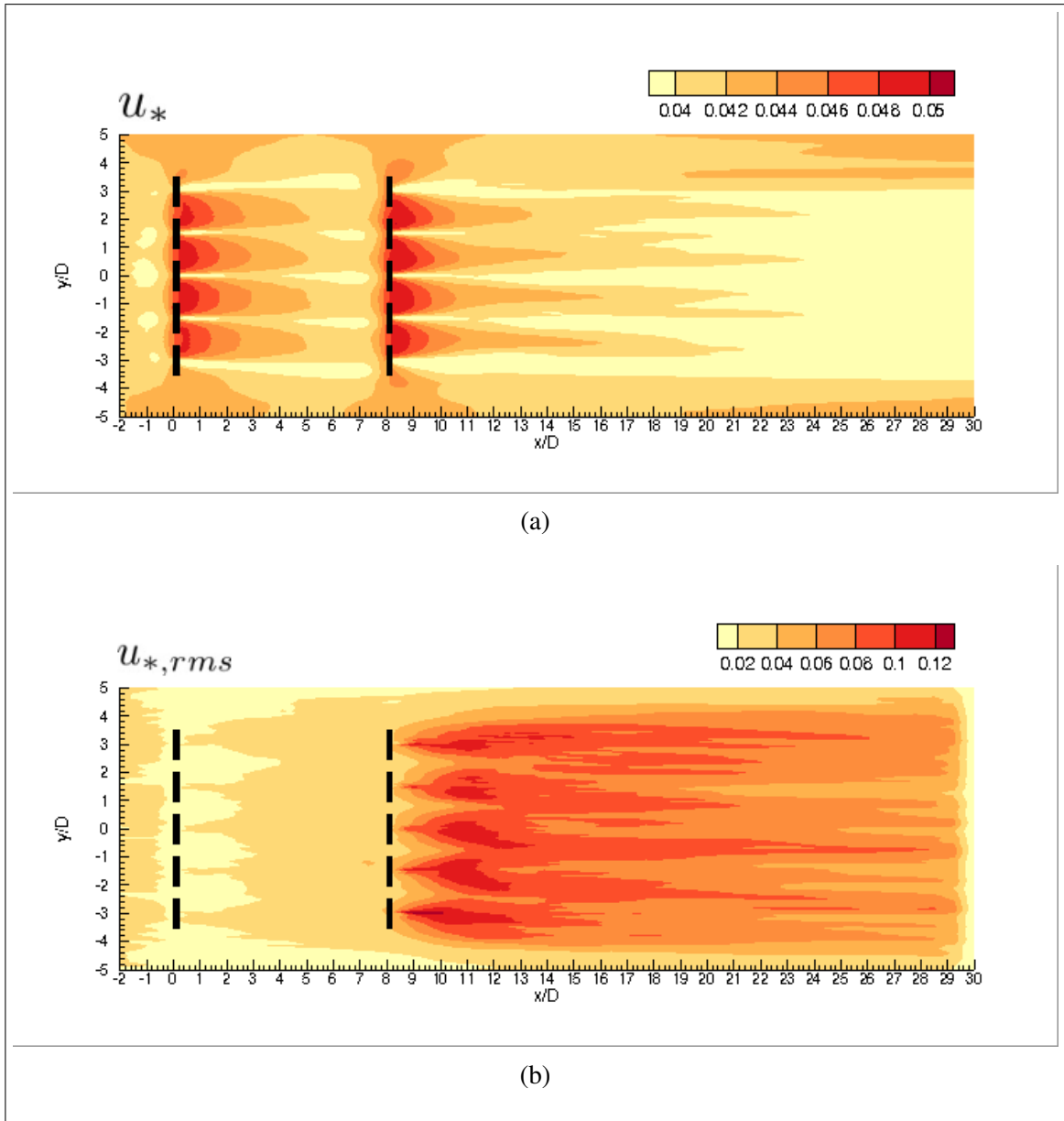


Figure 4.10. Contour plots of u_* and $u_{*,rms}$ for the ten turbine array: (a) time-averaged shear velocity, (b) shear velocity RMS.

4.2.4. Performance measurements

In order to grasp the bulk performance and power generation capability of tidal turbines it is common to use the power coefficient C_P as an indicator. As depicted in Figure 4.11, frontal devices showed results in the order of $C_P = 0.4$, in agreement of what was predicted by Stallard et al. (2013) and Thomson et al. (2011). The mean values for the power coefficient decrease in 20% and 50% for the staggered and aligned rows cases, respectively. This is a consequence of posterior devices having to face a flow which has already been extracted of momentum by upstream devices, and that their longitudinal spacing is not enough for the wake to recover completely. From the Figure it can also be clearly seen that increased velocity fluctuations associated with posterior rows have consequences in the temporal evolution of power generation for these devices. For example, the standard deviation of C_P for posterior rows was almost four times higher than the frontal row for the staggered row cases, and almost twice as high for the aligned rows case. To further understand the temporal variability of this performance variable we calculated the Coefficient of Variation C_V , defined as the ratio between the standard deviation σ and mean value μ of a data series (i.e.: $C_V = \sigma/\mu$). On average, in the aligned rows case C_V was more than 8 times higher for posterior devices, and almost 3 times higher for the staggered rows case.

Analyzing the coefficient of thrust C_T also gives an indication on overall turbine performance, specifically on the amount of thrust and loading a device will experience under its operation. Our results indicate the same type of behavior seen for C_P , frontal rows with good agreement to what was predicted experimentally, and posterior devices with lower values for the coefficient and considerably increased temporal variability, as seen in Figure 4.12. Posterior rows in the staggered array showed a 12% decrease in mean C_T , with a standard deviation and C_V , 3 and 4 times higher, respectively. In the aligned case, the mean values decreased in 20%, and had 2 and 3 times higher standard deviation and C_V , respectively.

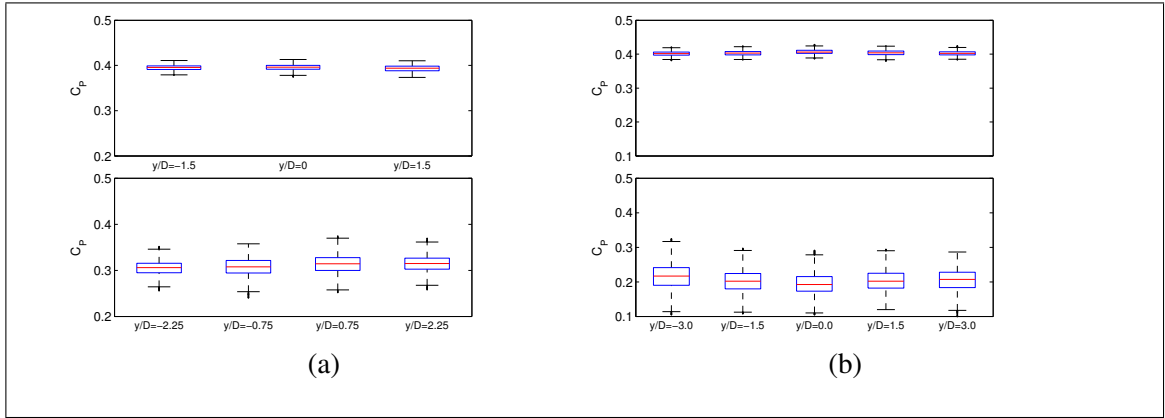


Figure 4.11. Box plots for C_P . Each box plot is obtained with the time-series of the respective turbine in the array. Superior plots are for frontal rows, and inferior for posterior ones. (a) two staggered rows; (b) two aligned rows.

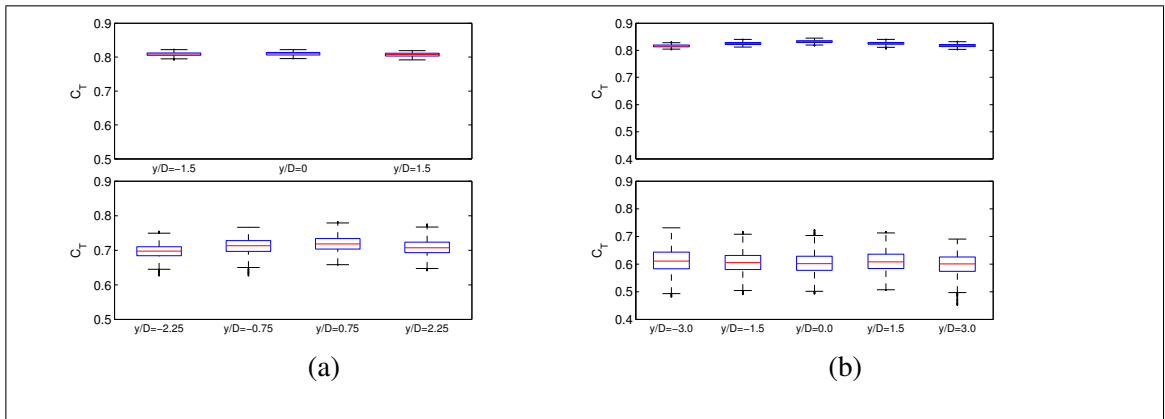


Figure 4.12. Box plots for C_T . Each box plot is obtained with the time-series of the respective turbine in the array. Superior plots are for frontal rows, and inferior for posterior ones. (a) two staggered rows; (b) two aligned rows.

All the results on C_T and C_P analyzed for both arrays can be found in Appendix E. It is interesting to note that the behavior when comparing with the URANS-BEM model is the same: as expected the second row of turbines always has lower thrust and power coefficients than the frontal one. However, the difference between rows is greater in our model. With DES-BEM posterior devices report, on average, results with C_T 15% and C_P 10% lower than URANS-BEM from Ingram & Olivieri (2012). This may be due to the

greater flow complexity and unsteadiness when using a more advanced turbulence model, and underscores the need to consider a possible overprediction of these coefficients when using simpler turbulence approximations. Comparing the studied arrays, temporal variability is higher and mean values are lower for the aligned rows case. Nevertheless, the scope of our study is not able to isolate the effect of the alignment of rows and the longitudinal spacing in the arrays, to understand which variable predominates in explaining these results. In order to do this, a more methodic approach can be followed, controlling such variables and then examining how they influence overall turbine performance and wake development.

From a turbine developer point of view the results discussed above are of critical importance, because they illustrate the fact that devices that interact with other turbine wakes will have considerably higher unsteadiness in its power generation capacity and also on turbine loading. The first aspect is relevant also for the reliability of electricity generation, bearing in mind that fluctuations in power output increase the overall cost of this type of technology. In terms of loading, temporal fluctuations can be associated with material fatigue, and therefore must be considered when making design decisions both for single devices and for array configurations.

5. CONCLUSIONS AND FUTURE WORK

The main objective of this study is to analyze the effect HATTs have on the flow surrounding them and improve the understanding about how these devices interact together when they are placed in an array. Additionally, we intend to validate a new approach for studying arrays of multiple tidal turbines, hopefully encouraging its use for further applications. In order to do this we coupled a DES flow solver based on the work by Escauriaza & Sotiropoulos (2011) and a BEM tidal turbine representation based on the work done by Creech et al. (2015). To incorporate ambient turbulence we added a Randow Flow Generator methodology, developed by Smirnov et al. (2001), to our inlet boundary condition. We apply the model to three different escenarios that were studied experimentally by Stalard et al. (2013) and Thomson et al. (2011), and numerically by Ingram & Olivieri (2012) using a BEM-URANS model.

We acknowledge that the proposed methodology considers a simplified tidal turbine representation, therefore it does not capture every dynamic feature of turbines wakes. Nevertheless, we show that it still can provide fundamental insights into the study of large tidal turbine arrays, whose demand on computational resources would be impractical if they were to be studied considering the exact geometry of the devices together with complex flow solvers such as DES.

The presented results allow us to conclude that coupling a detailed flow solver like DES with a low-order turbine model as BEM gives fundamental information on turbine array characterization. The model gave predictions on variables such as mean and instantaneous velocity fields, turbulence statistics, wake evolution and development, vortical structures on the flow, effects on the bed, and overall turbine performance measurements. Moreover, the model was able to represent rotational features in the wake which showed to dominate fundamental aspects of wake development and interaction. When comparing with a simpler turbulence model that had better geometrical representation of turbine hub

and nacelle, our results improved experimental predictions, while expanding the available information extractable from the results.

The comparison with the available data showed that our model was able to correctly predict the mean velocity distribution for every studied array. The region where bigger differences were appreciated was the near wake of turbines facing ambient flow (frontal rows and single devices), associated with our simplification of not considering the hub, nacelle and support structure geometry into the simulations. However, this difference is not seen in the wake of turbines located at posterior rows. Even in their near wake, the agreement with experiments was better than BEM-URANS with nacelle representation. Arguably, large scale structures produced by upstream devices dominate the evolution of the wake of downstream turbines, making geometrical simplifications and BEM limitations less relevant to predict mean velocity profiles. This underscores the advantages of using a detailed flow solver, like DES, even when it is coupled with low-order models like BEM.

Studying a single turbine on a flume it was shown that the studied device produces a longitudinal velocity deficit that lasts up to $20D$ downstream from it. This deficit is accompanied by changes in transversal velocity, vorticity, shear stresses and increased TKE in the wake region. Rotation in the wake was seen to decrease considerably near $5D$ downstream from the device, accompanied in an increase in TKE and Reynolds shear stress. Additionally, two vortex shedding regions were appreciated. First, BEM produces an annular vortex with the scale of the device diameter instead of tip-vortices in the outer region of the device. Second, downstream of the turbine hub a rotating vortex is produced. This latter vortex widens radially and interacts with the outer vortex around $5D$ downstream from the device, coinciding with the region of decreased rotation in the wake.

Regarding turbine arrays, it was shown that posterior rows face a more complex flow, with presence of vortices incoming from upstream devices. Higher unsteadiness and the presence of upstream turbulent structures accelerate the merging of individual device wakes into a single array wake. This array wake is characterized by higher turbulence

statistic levels and presence of large scale vortical structures. When analyzing bed shear velocity, results indicated that the region between devices - where flow acceleration exists - is characterized by higher shear stress and therefore can be considered a zone where scour is preferable. The contrary is true for regions behind turbine centers, where sediment deposition is more likely. In spite of the fact that mean values for u_* are similar for frontal and posterior rows, temporal fluctuations are up to five times higher in downstream rows, and owe up to a 10% variation from mean values. In terms of bulk turbine performance, it was shown that coefficients C_T and C_P not only decrease largely for turbines in posterior rows, but have considerably more temporal variation. This can have implications on turbine electricity generation capability and on device material wear and fatigue.

Future development of the model will include a more systematic approach for studying the effects of different array configurations, controlling variables such as device longitudinal and lateral spacing. Also, mesh refinement studies could be performed in order to fully understand and optimize the use of different grids to study tidal turbines with this DES-BEM approach. Moreover, the way the model was designed allows it to easily incorporate new geometries for non-ducted turbines, so it can be used to analyze and compare new types of HATTs designs on various array deployments. It is also of interest to incorporate the ability to simulate ducted turbines, expanding the spectrum of HATT types that can be addressed by our proposed model.

Additionally, in the long-term we aim to develop a robust methodology across temporal and spatial scales to characterize potential sites and analyze the impact of marine hydrokinetic devices. Therefore, we hope to use the model presented in this study in conjunction with models of different scope, complexity and scales, to gain further insight and opening new questions on the hydrodynamics feature associated with tidal energy generation.

REFERENCES

- Afgan, I., McNaughton, J., Rolfo, S., Apsley, D. D., Stallard, T., & Stansby, P. (2013). Turbulent flow and loading on a tidal stream turbine by LES and RANS. *International Journal of Heat and Fluid Flow*, *43*, 96–108. doi: 10.1016/j.ijheatfluidflow.2013.03.010
- Batten, W. M. J., Harrison, M. E., & Bahaj, A. (2013). Accuracy of the actuator disc-RANS approach for predicting the performance and wake of tidal turbines. *Philosophical transactions. Series A, Mathematical, physical, and engineering sciences*, *371*(1985), 20120293. doi: 10.1098/rsta.2012.0293
- Bennett, N. D., Croke, B. F. W., Guariso, G., Guillaume, J. H. A., Hamilton, S. H., Jakeman, A. J., ... Andreassian, V. (2013). Characterising performance of environmental models. *Environmental Modelling and Software*, *40*, 1–20. doi: 10.1016/j.envsoft.2012.09.011
- Blackmore, T., Batten, W. M. J., & Bahaj, A. (2014). Influence of turbulence on the wake of a marine current turbine simulator. *Proc. R. Soc. A*, *470*(20140331), 1–17. doi: 10.1098/rspa.2014.0331
- Bryden, I. G., & Couch, S. J. (2006). ME1 - Marine energy extraction: Tidal resource analysis. *Renewable Energy*, *31*(2), 133–139. doi: 10.1016/j.renene.2005.08.012
- Chamorro, L. P., Hill, C., Morton, S., Ellis, C., Arndt, R. E. A., & Sotiropoulos, F. (2013). On the interaction between a turbulent open channel flow and an axial-flow turbine. *Journal of Fluid Mechanics*, *716*, 658–670. doi: 10.1017/jfm.2012.571
- Chawdhary, S., Hill, C., Yang, X., Guala, M., Corren, D., Colby, J., & Sotiropoulos, F. (2017). Wake characteristics of a TriFrame of axial-flow hydrokinetic turbines. *Renewable Energy*. doi: 10.1016/j.renene.2017.03.029

- Churchfield, M., Li, Y., & Moriarty, P. (2013). A large-eddy simulation study of wake propagation and power production in an array of tidal-current turbines. *Philosophical transactions. Series A, Mathematical, physical, and engineering sciences*, 371(1985), 20120421. doi: 10.1098/rsta.2012.0421
- Creech, A., Borthwick, A., & Ingram, D. (2017). Effects of Support Structures in an LES Actuator Line Model of a Tidal Turbine with Contra-rotating Rotors. *Energies*, 10(726), 1–25. doi: 10.20944/preprints201703.0230.v1
- Creech, A., & Früh, W.-G. (2016). Modelling wind turbine wakes for wind farms. In J. Lehr (Ed.), *Alternative energy and shale gas encyclopedia* (chap. 4). doi: 10.1002/9781119066354.ch.4
- Creech, A., Früh, W. G., & Maguire, A. E. (2015). Simulations of an Offshore Wind Farm Using Large-Eddy Simulation and a Torque-Controlled Actuator Disc Model. *Surveys in Geophysics*, 36(3), 427–481. doi: 10.1007/s10712-015-9313-7
- Edenhofer, O., Pichs Madruga, R., & Sokona, Y. (2012). *Renewable Energy Sources and Climate Change Mitigation (Special Report of the Intergovernmental Panel on Climate Change)* (Vol. 6) (No. 4). doi: 10.5860/CHOICE.49-6309
- Edmunds, M., Williams, A. J., Masters, I., & Croft, T. N. (2017). An enhanced disk averaged CFD model for the simulation of horizontal axis tidal turbines. *Renewable Energy*, 101, 67–81. doi: 10.1016/j.renene.2016.08.007
- Escauriaza, C., & Sotiropoulos, F. (2011). Lagrangian model of bed-load transport in turbulent junction flows. *Journal of Fluid Mechanics*, 666, 36–76. doi: Doi 10.1017/S0022112010004192
- Gaurier, B., Davies, P., Deuff, A., & Germain, G. (2013). Flume tank characterization of marine current turbine blade behaviour under current and wave loading. *Renewable Energy*, 59, 1–12. doi: 10.1016/j.renene.2013.02.026

Hill, C., Musa, M., Chamorro, L. P., Ellis, C., & Guala, M. (2014). Local Scour around a Model Hydrokinetic Turbine in an Erodible Channel. *Journal of Hydraulic Engineering*, 140(8), 0414037. doi: 10.1061/(ASCE)HY.1943-7900.0000900.

Hill, C., Musa, M., & Guala, M. (2016). Interaction between instream axial flow hydrokinetic turbines and uni-directional flow bedforms. *Renewable Energy*, 86, 409–421. doi: 10.1016/j.renene.2015.08.019

Hunt, J. C. R., Wray, a. a., & Moin, P. (1988). Eddies, streams, and convergence zones in turbulent flows. *Center for Turbulence Research, Proceedings of the Summer Program(1970)*, 193–208. doi: CTR-S88

Ingram, D., & Olivieri, D. A. (2012). *Tidal array scale numerical modelling. Interactions within a farm (Steady Flow). PerAWaT MA1003 Deliverable WG3 WP2 D5a* (Tech. Rep.). Edinburgh: Energy Technologies Institute.

Kalitzin, G., Medic, G., Iaccarino, G., & Durbin, P. (2005). Near-wall behavior of RANS turbulence models and implications for wall functions. *Journal of Computational Physics*, 204(1), 265–291. doi: 10.1016/j.jcp.2004.10.018

Kang, S., Yang, X. L., & Sotiropoulos, F. (2014). On the onset of wake meandering for an axial flow turbine in a turbulent open channel flow. *Journal of Fluid Mechanics*, 744(2014), 376–403. doi: Doi 10.1017/Jfm.2014.82

Khan, M., Bhuyan, G., Iqbal, M., & Quaicoe, J. (2009, oct). Hydrokinetic energy conversion systems and assessment of horizontal and vertical axis turbines for river and tidal applications: A technology status review. *Applied Energy*, 86(10), 1823–1835. doi: 10.1016/j.apenergy.2009.02.017

Lloyd, T. P., Turnock, S. R., & Humphrey, V. F. (2014). Assessing the influence of inflow turbulence on noise and performance of a tidal turbine using large eddy simulations. *Renewable Energy*, 71, 742–754. doi: 10.1016/j.renene.2014.06.011

Lynn, P. A. (2014). *Electricity From Wave and Tide: An Introduction to Marine Energy* (1st ed.). Chichester: Wiley.

Magagna, D., & Uihlein, A. (2015). Ocean energy development in Europe: Current status and future perspectives. *International Journal of Marine Energy*, *11*, 84–104. doi: 10.1016/j.ijome.2015.05.001

Maganga, F., Germain, G., King, J., Pinon, G., & Rivoalen, E. (2009). Experimental study to determine flow characteristic effects on marine current turbine behaviour. *8th European Wave and Tidal Energy Conference*, *4*(May), 661–667. doi: <http://dx.doi.org/10.1049/iet-rpg.2009.0205>

Malki, R., Masters, I., Williams, A. J., & Croft, T. N. (2013). The variation in wake structure of a tidal stream turbine with flow velocity. In L. Eca, E. Oñate, J. García-Espinosa, T. Kvamsdal, & P. Bergan (Eds.), *Computational methods in applied sciences* (Vol. 29, pp. 137–148). Dordrecht: Springer Science + Business Media. doi: 10.1007/978-94-007-6143-8_8

Masters, I., Chapman, J. C., Willis, M. R., & Orme, J. A. C. (2011). A robust blade element momentum theory model for tidal stream turbines including tip and hub loss corrections. *Journal of Marine Engineering and Technology*, *10*(1). doi: 10.1080/20464177.2011.11020241

Masters, I., Malki, R., Williams, A. J., & Croft, T. N. (2013). The influence of flow acceleration on tidal stream turbine wake dynamics: A numerical study using a coupled BEM-CFD model. *Applied Mathematical Modelling*, *37*(16-17), 7905–7918. doi: 10.1016/j.apm.2013.06.004

Masters, I., Williams, A. J., Croft, T., Togneri, M., Edmunds, M., Zangiabadi, E., ... Karunarathna, H. (2015, jul). A Comparison of Numerical Modelling Techniques for Tidal Stream Turbine Analysis. *Energies*, *8*, 7833–7853. doi: 10.3390/en8087833

- Mycek, P., Gaurier, B., Germain, G., Pinon, G., & Rivoalen, E. (2014a). Experimental study of the turbulence intensity effects on marine current turbines behaviour. Part II: Two interacting turbines. *Renewable Energy*, *68*, 876–892. doi: 10.1016/j.renene.2013.12.048
- Mycek, P., Gaurier, B., Germain, G., Pinon, G., & Rivoalen, E. (2014b). Experimental study of the turbulence intensity effects on marine current turbines behaviour. Part I: One single turbine. *Renewable Energy*, *66*, 729–746. doi: 10.1016/j.renene.2013.12.036
- Myers, L. E., & Bahaj, A. (2012). An experimental investigation simulating flow effects in first generation marine current energy converter arrays. *Renewable Energy*, *37*(1), 28–36. doi: 10.1016/j.renene.2011.03.043
- Nguyen, V. T., Guillou, S. S., Thiebot, J., & Cruz, A. S. (2016). Modelling turbulence with an Actuator Disk representing a tidal turbine. *Renewable Energy*, *97*, 625–635. doi: 10.1016/j.renene.2016.06.014
- Paik, J., Escauriaza, C., & Sotiropoulos, F. (2010). Coherent structure dynamics in turbulent flows past in-stream structures: Some insights gained via numerical simulation. *Journal of Hydraulic Engineering*, *136*(12), 981–993. doi: doi:10.1061/(ASCE)HY.1943-7900.0000089
- Paik, J., Sotiropoulos, F., & Sale, M. J. (2005). Numerical Simulation of Swirling Flow in Complex Turbulence Models. *Journal of Hydraulic Engineering*, *131*(June), 441–456.
- Pinon, G., Mycek, P., Germain, G., & Rivoalen, E. (2012). Numerical simulation of the wake of marine current turbines with a particle method. *Renewable Energy*, *46*, 111–126. doi: 10.1016/j.renene.2012.03.037
- Polagye, B., Cleve, B. V., Kirkendall, K., & Copping, A. (2010). Environmental effects of tidal energy development. In *Proceedings of a scientific workshop*.

- Riglin, J., Chris Schleicher, W., Liu, I. H., & Oztekin, A. (2015). Characterization of a micro-hydrokinetic turbine in close proximity to the free surface. *Ocean Engineering*, *110*, 270–280. doi: 10.1016/j.oceaneng.2015.10.026
- Smirnov, A., Shi, S., & Celik, I. (2001). Random Flow Generation Technique for Large Eddy Simulations and Particle-Dynamics Modeling. *Journal of Fluids Engineering*, *123*(2), 359. doi: 10.1115/1.1369598
- Spalart, P. R. (2009). Detached-Eddy Simulation. *Annual Review of Fluid Mechanics*, *41*(1), 181–202. doi: 10.1146/annurev.fluid.010908.165130
- Spalart, P. R., & Allmaras, S. R. (1994). A one-equation turbulence model for aerodynamic flows. *La Recherche Aéronautique*, *1*, 5–21.
- Spalart, P. R., Jou, W.-H., Strelets, M., & Allmaras, S. R. (1997). Comments on the feasibility of LES for wings, and on a hybrid RANS/LES approach. In C. Liu & Z. Liu (Eds.), *Advances in dns/les* (pp. 138–147). Ruston: Greyden Press.
- Stallard, T., Collings, R., Feng, T., & Whelan, J. (2013). Interactions between tidal turbine wakes: Experimental study of a group of three-bladed rotors. *Philosophical Transactions of the Royal Society A*, *371*(1985), 1471–2962.
- Tabor, G. R., & Baba-Ahmadi, M. H. (2010). Inlet conditions for large eddy simulation: A review. *Computers and Fluids*, *39*(4), 553–567. doi: 10.1016/j.compfluid.2009.10.007
- Thomson, M., Collings, R., & Stallard, T. (2011). *Array Scale Experimental Test Report. PerAWaT Deliverable MA1003 WG4 WP2 D5* (Tech. Rep.). Manchester: Energy Technologies Institute.
- Uihlein, A., & Magagna, D. (2016). Wave and tidal current energy - A review of the current state of research beyond technology. *Renewable and Sustainable Energy Reviews*, *58*, 1070–1081. doi: 10.1016/j.rser.2015.12.284

Yuce, M. I., & Muratoglu, A. (2010). Hydrokinetic energy conversion systems: A technology status review. *Renewable and Sustainable Energy Reviews*, *14*(9), 2996–3004. doi: 10.1016/j.rser.2010.06.016

APPENDIX

A. RANDOM FLOW GENERATION TECHNIQUE

To generate a time dependant flow field that represents realistic conditions of whatever situation we wish to modelate, we follow the Random Flow Generation (RFG) technique proposed by Smirnov et al. (2001). The steps to do this are the following:

- (i) Diagonalize the velocity correlation tensor:

Given any anisotropic velocity correlation tensor

$$r_{ij} = \overline{u_i u_j} \quad (\text{A.1})$$

obtain an orthogonal transformation tensor a_{ij} for diagonalizing r_{ij}

$$a_{mi} a_{nj} r_{ij} = d_{mn} c_{(n)}^2 \quad (\text{A.2})$$

$$a_{ik} a_{kj} = \delta_{ij} \quad (\text{A.3})$$

In the new coordinate system represented by the tensor a_{ij} , the coefficients $c_n = \{c_1, c_2, c_3\}$ represent the fluctuating velocities (u', v', w').

- (ii) Generate a transient flow-field:

For every point and time (\vec{x}, t) where the RFG technique will be applied use the following function for generating a velocity series $v_i(\vec{x}, t)$:

$$v_i(\vec{x}, t) = \sqrt{\frac{2}{N}} \sum_{n=1}^N \left[p_i^n \cos(\tilde{k}_j^n \tilde{x}_j + \omega_n \tilde{t}) + q_i^n \sin(\tilde{k}_j^n \tilde{x}_j + \omega_n \tilde{t}) \right] \quad (\text{A.4})$$

$$\tilde{x}_j = \frac{x_j}{l}, \tilde{t} = \frac{t}{\tau}, c = \frac{l}{\tau}, \tilde{k}_j^n = k_j^n \frac{c}{c_{(j)}} \quad (\text{A.5})$$

$$p_i^n = \epsilon_{ijm} \zeta_j^n k_m^n, q_i^n = \epsilon_{ijm} \xi_j^n k_m^n \quad (\text{A.6})$$

$$\zeta_i^n, \xi_i^n, \omega_n \in N(0, 1), k_i^n \in N(0, 1/2) \quad (\text{A.7})$$

where l, τ are length- and time-scales of turbulence, ϵ_{ijk} is the permutation tensor and $N(M, \sigma)$ is a normal distribution with M and σ as mean and standard deviation, respectively. The numbers k_j^n, ω_n are a sample of n wave-numbers and frequencies, respectively, of the turbulence spectrum

$$E(k) = 16 \left(\frac{2}{\pi} \right)^{1/2} k^4 \exp(-2k^2) \quad (\text{A.8})$$

(iii) Scale the flow-field:

To obtain a new flow-field u_i in the original coordinate system we apply a the following scaling and orthogonal transformation to the results obtained above:

$$w_i = c_{(i)} v_{(i)} \quad (\text{A.9})$$

$$u_i = a_{ik} w_k \quad (\text{A.10})$$

As a summary, the RFG method takes the original correlation tensor r_{ij} and turbulence length- and time-scales, (l, τ) , as inputs. As an output it delivers a time-dependent flow-field $u_i(x_j, t)$.

In our implementation for the PerAWaT case study, we assume an isotropic correlation tensor at the flume's inlet, with magnitudes of fluctuation as reported by Thomson et al. (2011):

$$\begin{bmatrix} TI_x \\ TI_y \\ TI_z \end{bmatrix} = \begin{bmatrix} 0.1 \\ 0.09 \\ 0.08 \end{bmatrix} \quad (\text{A.11})$$

Additionally, following Smirnov et al. (2001), we use $N = 1000$ for sampling. The characteristic length scale l for every mesh node in the inlet was defined as 0.1 times the node's wall distance coefficient used in DES:

$$l = 0.1 \min \{d, 0.65\Delta\} \quad (\text{A.12})$$

where d is the distance to the closest wall and Δ is the largest grid spacing nearest to the node $\Delta = \max \{ \Delta_x, \Delta_y, \Delta_z \}$.

Finally, considering that the fundamental fluctuations are in the longitudinal direction, the time scale was built using TI_x as a reference:

$$\tau = \frac{l}{TI_x} \tag{A.13}$$

B. FLOW STATISTICS FOR THE ALIGNED ROWS CASE

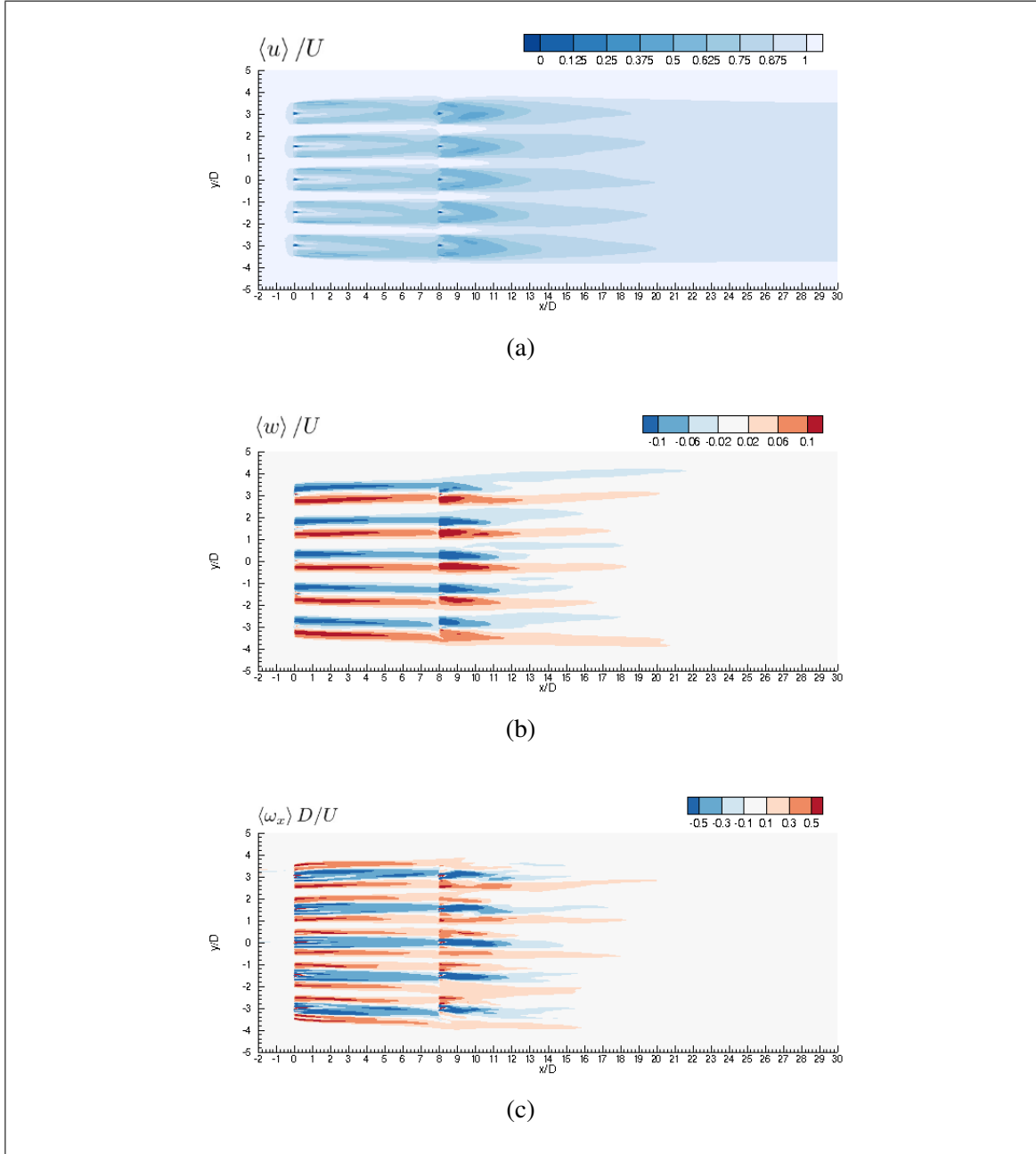


Figure B.1. Contour plots of mean flow statistics at a horizontal plane at $z/D = 0$ for the aligned rows case: (a) non-dimensional mean longitudinal velocity; (b) non-dimensional mean vertical velocity; (c) non-dimensional mean axial vorticity.

C. TURBULENCE STATISTICS FOR THE STAGGERED ROWS CASE

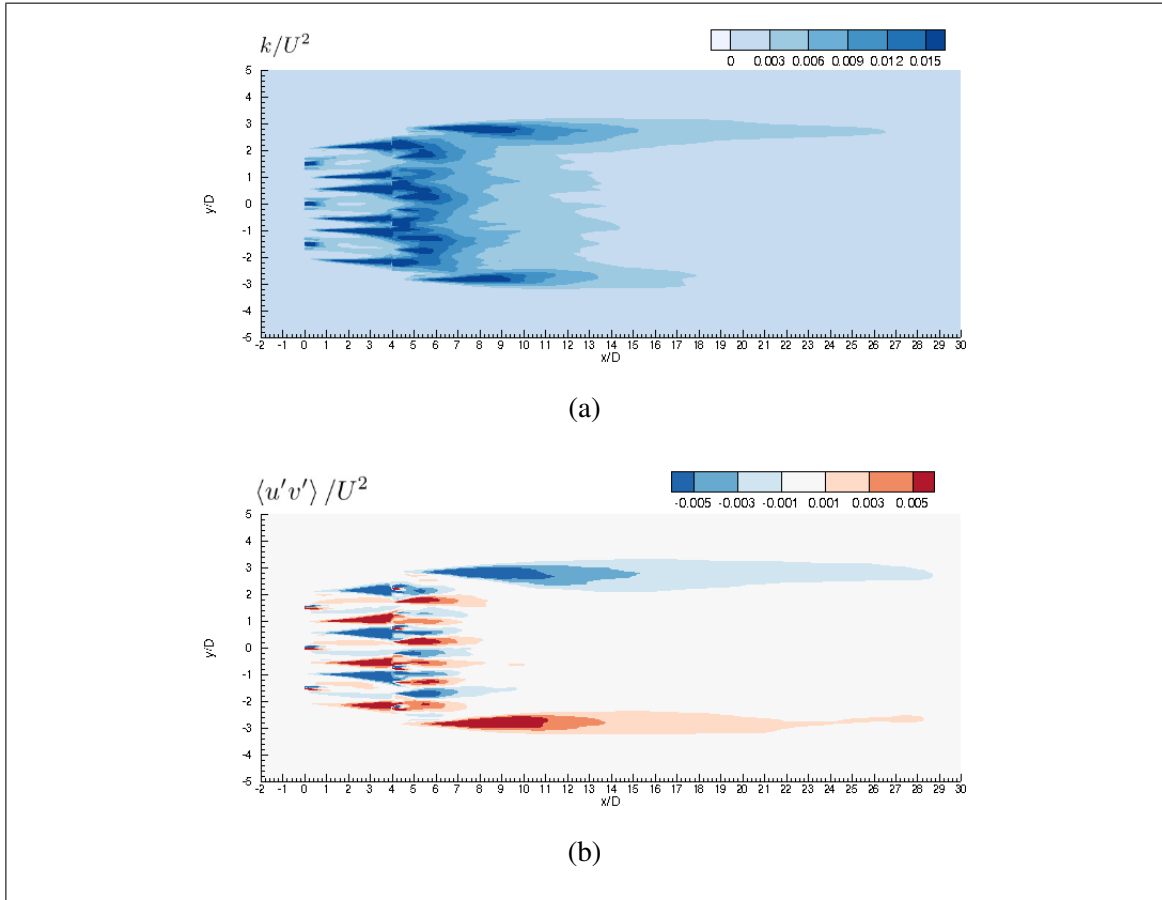


Figure C.1. Contour plots of turbulence statistics at a horizontal plane at $z/D = 0$ for the staggered rows case: (a) non-dimensional TKE; (b) non-dimensional principal Reynolds shear stress.

D. EFFECTS ON THE BED FOR THE STAGGERED ROWS ARRAY

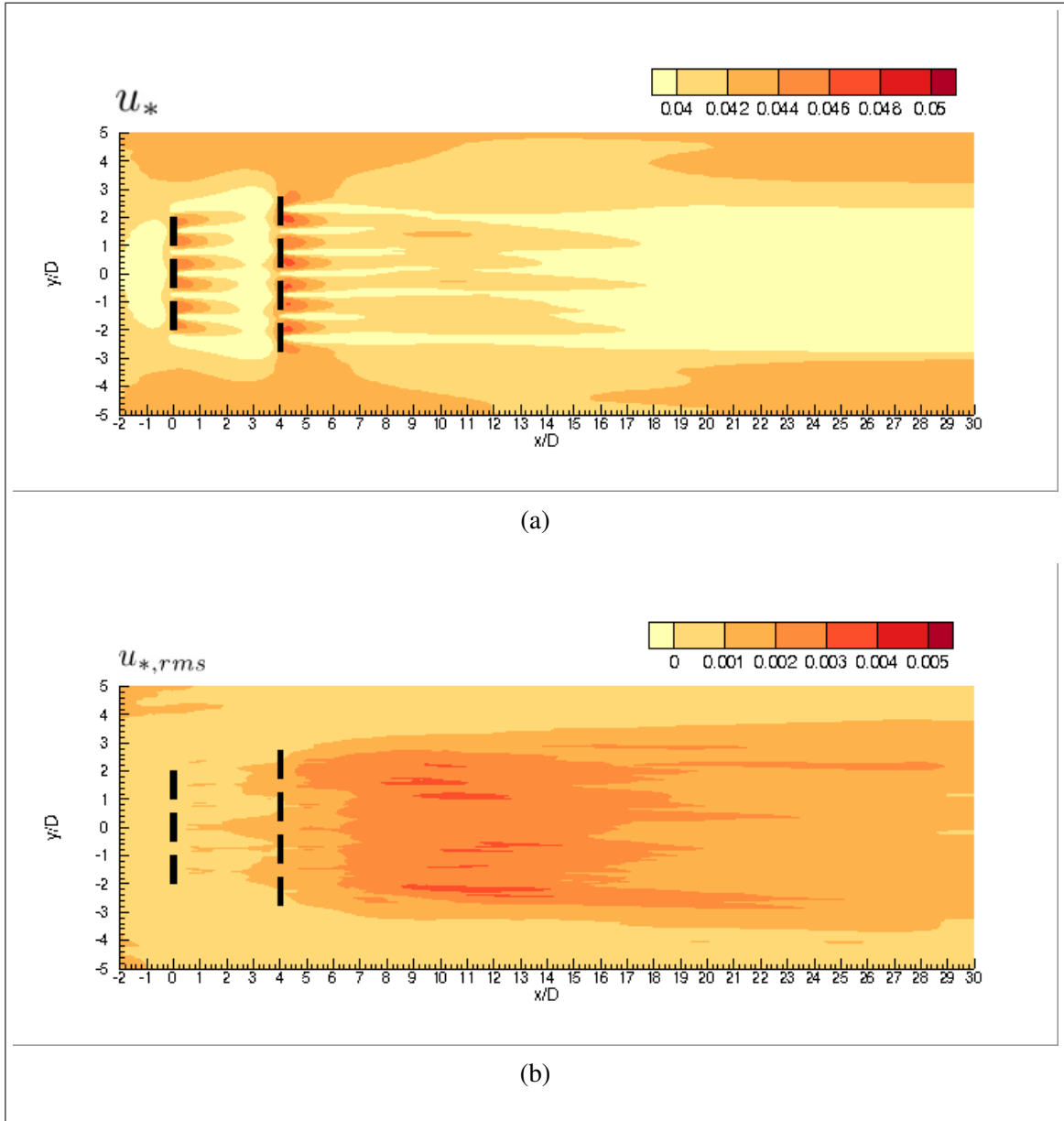


Figure D.1. Contour plots of u_* and $u_{*,rms}$ for the staggered rows array: (a) time-averaged shear velocity, (b) shear velocity RMS.

E. TURBINE PERFORMANCE FOR DOUBLED ROW ARRAYS

Table E.1. Turbine performance results for the two double row arrays. Statistics are obtained averaging the desired variable for every device on the same row. The comparison between arrays is performed by calculating the ratio between the variability of both arrays.

		C_T					C_P				
		Mean	Max.	Min.	σ	C_V	Mean	Max.	Min.	σ	C_V
Staggered	Frontal row	0.81	0.82	0.79	0.005	0.01	0.39	0.41	0.38	0.006	0.02
	Posterior row	0.71	0.77	0.64	0.022	0.03	0.31	0.36	0.25	0.018	0.06
	$\Delta\%$	-12%	-6%	-20%	331%	392%	-21%	-12%	-33%	190%	269%
Aligned	Frontal row	0.82	0.84	0.81	0.005	0.01	0.40	0.42	0.38	0.007	0.02
	Posterior row	0.61	0.72	0.48	0.039	0.06	0.20	0.30	0.10	0.033	0.16
	$\Delta\%$	-26%	-15%	-40%	673%	951%	-49%	-30%	-73%	382%	851%
$\Delta\%$ between arrays		47%	43%	49%	49%	41%	44%	40%	45%	50%	32%